JCB Journal of Cell Biology

ARTICLE

The Orf9b protein of SARS-CoV-2 modulates mitochondrial protein biogenesis

Svenja Lenhard[1*], Sarah Gerlich[2,4*], Azkia Khan[1], Saskia Rödl[1], Jan-Eric Bökenkamp[3], Esra Peker[2,4], Christine Zarges[2,4], Janina Faust[1], Zuzana Storchova[3], Markus Räschle[3], Jan Riemer[2,4], and Johannes M. Herrmann[1]

The severe acute respiratory syndrome coronavirus 2 (SARS-CoV-2) expresses high amounts of the protein Orf9b to target the mitochondrial outer membrane protein Tom70. Tom70 serves as an import receptor for mitochondrial precursors and, independently of this function, is critical for the cellular antiviral response. Previous studies suggested that Orf9b interferes with Tom70-mediated antiviral signaling, but its implication for mitochondrial biogenesis is unknown. In this study, we expressed Orf9b in human HEK293 cells and observed an Orf9b-mediated depletion of mitochondrial proteins, particularly in respiring cells. To exclude that the observed depletion was caused by the antiviral response, we generated a yeast system in which the function of human Tom70 could be recapitulated. Upon expression of Orf9b in these cells, we again observed a specific decline of a subset of mitochondrial proteins and a general reduction of mitochondrial volume. Thus, the SARS-CoV-2 virus is able to modulate the mitochondrial proteome by a direct effect of Orf9b on mitochondrial Tom70-dependent protein import.

Introduction

Mitochondria are essential organelles of eukaryotic cells. They play pivotal roles in the production of ATP and carry out a multitude of metabolic reactions, including the synthesis of iron–sulfur clusters, amino acids, and lipids. In addition to their central role in metabolism, mitochondria serve as a hub in cellular signaling reactions. Well-studied examples are the intrinsic apoptosis pathway triggered by the mitochondrial release of cytochrome c, or the antiviral signaling of the innate immune response triggered by the release of mitochondrial DNA and by activation of the mitochondrial antiviral signaling (MAVS) protein (Jacobs and Coyne, 2013; Kasahara and Scorrano, 2014; McWhirter et al., 2005; Moehlman and Youle, 2020).

Proteins of the mitochondrial surface are of central relevance in all these reactions as they serve as an interface between mitochondria and non-mitochondrial compartments of the cell. Tom70 (which we spell here consistently Tom70 for simplicity even when we refer to the mammalian TOM70/TOMM70 ortholog) is particularly important in this context (Kreimendahl and Rassow, 2020): Tom70 binds to internal targeting signals in nucleus-encoded mitochondrial precursor proteins (Fig. 1 A) and facilitates their import from the cytosol through the TOM complex into mitochondria (Backes et al., 2018; Hase et al., 1983; Hines and Schatz, 1993; Komiya et al., 1997; Schlossmann et al., 1994; Suzuki et al., 2002). In addition, Tom70 contains a defined binding site for cytosolic chaperones of the Hsp70 and Hsp90 family and also interacts with the J protein Djp1. Together with these chaperones, Tom70 facilitates the local unfolding and posttranslational import of precursor proteins into mitochondria (Backes et al., 2021; Opaliński et al., 2018; Yamamoto et al., 2009; Young et al., 2003). Moreover, Tom70 serves as binding site for contact sites with the endoplasmic reticulum (ER; Eisenberg-Bord et al., 2021; Filadi et al., 2018; Murley et al., 2015) and for quality control components (Li et al., 2022; Liu et al., 2022; Mårtensson et al., 2019; Weidberg and Amon, 2018). These general functions of Tom70 in mitochondrial biogenesis are presumably of universal relevance in animals and fungi. In human cells, Tom70 plays an additional, animal-specific important role in antiviral signaling: Upon infection with RNA viruses, human Tom70 is critical for the oligomerization and activation of the MAVS protein, as well as for the recruitment of the Hsp90-bound interferon regulatory factor 3 and the TANK-binding kinase 1 to the mitochondrial surface, where interferon regulatory factor 3 is phosphorylated and passed on to the

[1]Cell Biology, University of Kaiserslautern, Kaiserslautern, Germany; [2]Biochemistry, University of Cologne, Cologne, Germany; [3]Molecular Genetics, University of Kaiserslautern, Kaiserslautern, Germany; [4]CECAD, University of Cologne, Cologne, Germany.

*S. Lenhard and S. Gerlich contributed equally to this paper. Correspondence to Johannes M. Herrmann: hannes.herrmann@biologie.uni-kl.de; Jan Riemer: jan.riemer@uni-koeln.de.

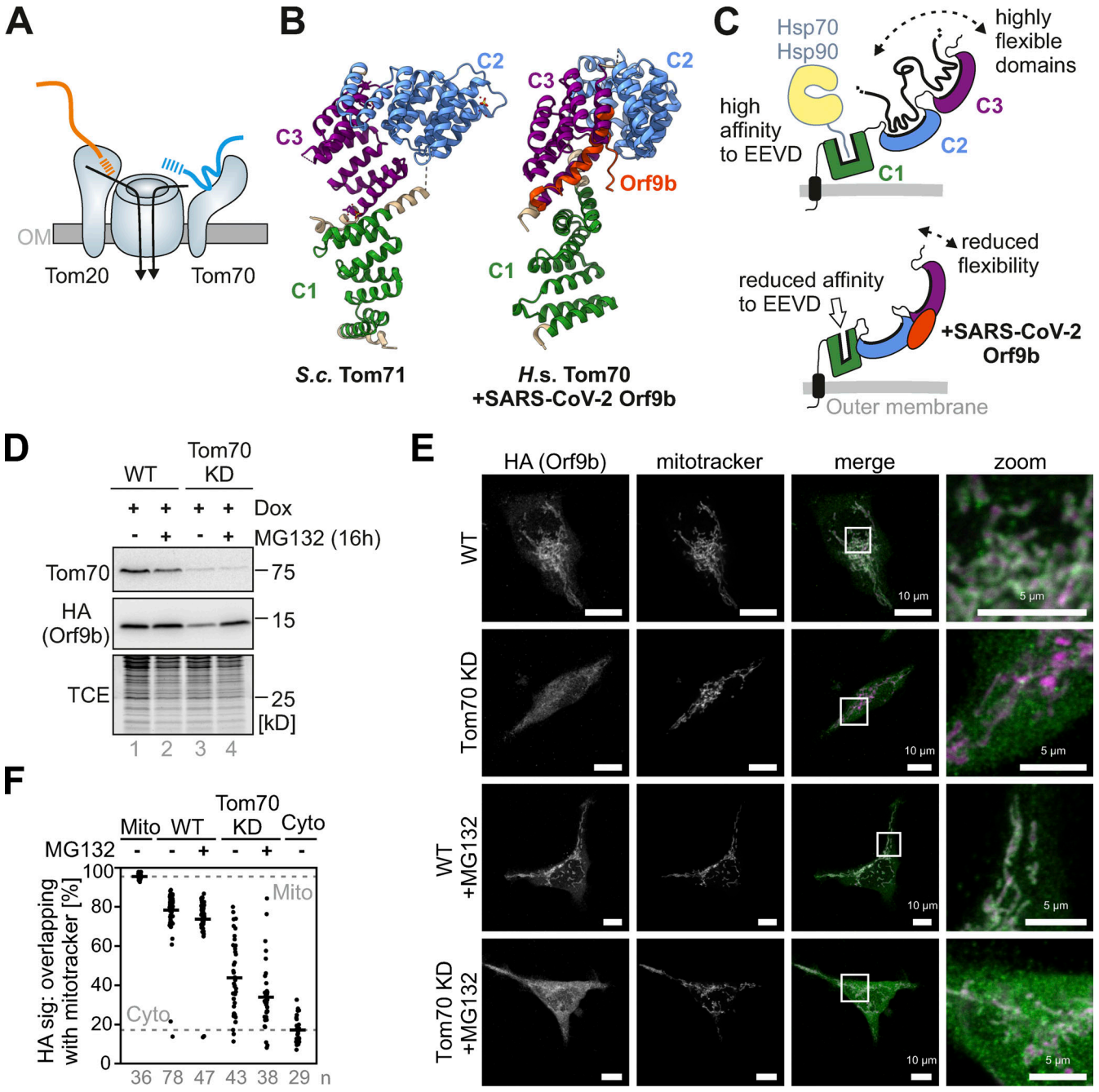

Figure 1. **In human cells, Orf9b binds to mitochondria in a Tom70-dependent manner. (A)** Schematic representation of the import pore in the mitochondrial outer membrane (OM). The structure was highly simplified, neglecting its overall organization with two or three translocation pores. Note that Tom20 and Tom70 represent two receptors for precursor proteins that cooperate in protein recognition. **(B)** The cytosolic domain of Tom70 consists of 27 α-helices that constitute 11 TPR domains. The N-terminal membrane anchor is not shown here. Shown are the structures of yeast Tom71 (PDB: 3FP3; Li et al., 2010) and of the human Tom70 bound to Orf9b (PDB: 7KDT; Gao et al., 2021). The C1 (clamp), C2 (core), and C3 (C-terminal) domains are shown in green, blue, and violet, respectively. **(C)** Schematic representation of the structural consequences of the Orf9b binding to Tom70. Tom70 is anchored to the outer membrane by an N-terminal transmembrane domain (shown in black). The C1 domain serves as binding site for the C-terminal EEVD peptides of cytosolic Hsp70 and Hsp90 chaperones (Backes et al., 2018; Li et al., 2009; Young et al., 2003). The C2 and C3 domains serve as binding sites to mitochondrial precursor proteins, in particular to carrier proteins and proteins with internal matrix-targeting sequences. Orf9b binds to the C2–C3 regions and was proposed to reduce their dynamic flexibility (Gao et al., 2021). **(D)** Orf9b-HA was expressed upon doxycycline (Dox) addition in HEK293 WT or CRISPR-Cas9 mediated *Tom70* knockdown cells. In the lanes indicated with MG132, the activity of the proteasome was inhibited for 16 h. Samples were analyzed by Western blotting with Tom70 and HA-specific antibodies. A total cell extract labeling with TCE is shown for control. Please note that the proteasomal stability of Orf9b depends on the presence of Tom70. Orf9b was expressed in all four lanes of this experiment. **(E)** Cells were grown as described in C, fixated, and analyzed by fluorescence microscopy. Representative examples of cells are shown. Please note, that the colocalization of Orf9b and mitochondria (shown as white signals in the merged figures) depends on the presence of Tom70. Inhibition of the proteasomal protein degradation in the cytosol for 2 h by MG132 increases the non-mitochondrial levels of Orf9b. **(F)** Quantitative analysis of the colocalization of Orf9b-HA and MitoTracker. The colocalization was quantified using Fiji and Just Another Co-

localization Plugin. The values shown represent the Manders' overlap coefficient (M1) for single cells. The numbers of analyzed cells (i.e., technical replicates) are indicated in the plot. Su9-MTS-roGFP2 and roGFP2-NES were shown as references for mitochondrial and cytosolic staining, respectively (Fig. S1 D). Source data are available for this figure: SourceData F1.

nucleus to trigger the antiviral innate immune response (Liu et al., 2010; Shi et al., 2014).

Owing to these multiple functions, Tom70 exposes several distinct binding sites for different interactors and is of highly flexible structure (Kondo-Okamoto et al., 2008; Suzuki et al., 2002; Wu and Sha, 2006; Zanphorlin et al., 2016); however, the architecture of Tom70 and the spatial organization of its binding sites for these different ligands are poorly characterized. Tom70 proteins of animals and fungi consist of an N-terminal outer membrane anchor followed by 11 tetratricopeptide repeat (TPR) domains (Chan et al., 2006; Li et al., 2010). The first three TPR domains form a binding site for the C-terminal EEVD peptide of cytosolic Hsp70 and Hsp90 chaperones (clamp domain or C1; Young et al., 2003), followed by a less defined region that directly interacts with mitochondrial-precursor proteins (core and C-terminal part, C2 and C3; Fig. 1 B). Many of these precursor proteins have internal regions with structural similarity to mitochondrial targeting signals (internal matrix-targeting signal-like [iMTS] sequences) that can be predicted by algorithms such as targetP (Backes et al., 2018; Boos et al., 2018; Schneider et al., 2021).

Several viruses express proteins to interfere with Tom70 function as a strategy to modulate mitochondrial activities and to suppress antiviral signaling (Brandherm et al., 2021; Burtscher et al., 2021; Gao et al., 2021; Jiang et al., 2020; Neufeldt et al., 2022; Wong and Perlman, 2022). Most prominently, the SARS-CoV-2 virus expresses from an alternative reading frame the 11-kD protein, Orf9b, which is one of the most abundant viral proteins in infected cells and was found to bind to Tom70 (Gao et al., 2021; Jiang et al., 2020; Miserey-Lenkei et al., 2021). Orf9b associates with a region on the C2/C3 substrate binding domain of Tom70, while it does presumably not directly occupy the precursor-binding and chaperone-binding clefts. In vitro, data indicate that it impairs the flexibility of Tom70 and compromises the chaperone recruitment to the C1 domain by allosteric modulations of its structure (Fig. 1, B and C; Brandherm et al., 2021; Gao et al., 2021). Thereby, Orf9b targeting Tom70 prevents MAVS oligomerization and activation on the mitochondrial surface and sabotages the antiviral signaling in cells infected with SARS-CoV-2. More evolved forms of the virus such as the Delta or Omicron variants even improved the Orf9b binding to Tom70, which apparently is a crucial element in their enhanced immune evasion (Hossain et al., 2022; Thorne et al., 2022; Wu et al., 2021).

While several recent studies characterized the Orf9b-mediated inhibition of MAVS binding to Tom70, it is unclear whether Orf9b expression also influences the housekeeping function of Tom70 in mitochondrial protein import. We therefore tested whether Orf9b expression influences the proteome in human cells. We found that Orf9b expression specifically reduces the abundance of mitochondrial proteins. Strikingly, most of these proteins (76%) show a similar decrease upon knockdown of Tom70, suggesting that Orf9b jeopardizes Tom70-mediated protein import. To exclude indirect effects of Orf9b expression in these cells, for example, via components of the antiviral response, we generated yeast cells (lacking any antiviral signaling system) expressing a "humanized" Tom70 protein. The expression of Orf9b in these cells again reduced the import of Tom70 substrates, an effect that was also confirmed by in vitro import assays with semi-intact cells. As a consequence of this import inhibition, Orf9b expression induces a general decline in mitochondrial volume. Our study, therefore, shows that Orf9b expression not only interferes with the antiviral response in SARS-CoV-2–infected cells but also has the capacity to directly modulate mitochondrial biogenesis.

Results

Orf9b binds to mitochondria in a Tom70-dependent manner

Recent proteomic studies revealed that the infection with SARS-CoV-2 virus causes mitochondrial dysfunction and the selective depletion of mitochondrial proteins (Bhowal et al., 2022; Bojkova et al., 2020; Chang et al., 2022; Denaro et al., 2022; Gibellini et al., 2020; Shi et al., 2014; Stukalov et al., 2021; Surendran et al., 2022). Tom70 contains distinct binding sites for mitochondrial precursor proteins and for Hsp70/Hsp90 chaperones, both of which were proposed to be affected by Orf9b binding owing to a general stiffening of the Tom70 structure (Fig. 1 C). The changes in the mitochondrial proteome might be induced by these changes in Tom70-mediated protein import; however, they also might stem from more pleiotropic consequences of the infection and concomitant anti-viral responses of the host cell. To selectively study the effect of Orf9b, we generated a HEK293 cell-based model, which allowed the doxycycline-induced expression of Orf9b (equipped with a C-terminal HA tag) in a WT and CRISPR-Cas9 mediated *Tom70* knock-down background (Fig. S1 A). Knockdown of *Tom70* showed diminished levels of Orf9b (Fig. 1 D) whereas Orf9b expression had no consistent influence on Tom70 levels. The reduction of Orf9b was presumably caused by the proteolytic instability of the non-bound Orf9b, as inhibition of the proteasome by MG132 treatment prevented the Orf9b depletion. This is consistent with previous reports about the critical relevance of Tom70 for the binding and stabilization of Orf9b (Brandherm et al., 2021; Gao et al., 2021; Jiang et al., 2020; Miserey-Lenkei et al., 2021; Shi et al., 2014). Mitochondria isolated from Orf9b-expressing cells were still associated with cytosolic chaperones such as Hsp70 and Hsp90, suggesting that mitochondria—as expected—also expose other, Tom70-independent chaperone binding sites on their surface (Fig. S1, B and C).

Next, we visualized the distribution of Orf9b and mitochondria by fluorescence microscopy (Fig. 1 E and Fig. S1 D). Orf9b colocalized with mitochondria in a Tom70-dependent manner. Upon depletion of Tom70 and proteasome inhibition

with MG132, Orf9b was distributed throughout the cell and its mitochondrial localization was abolished (Fig. 1 F). Thus, the HEK293 cell model recapitulates the Tom70-dependent recruitment of Orf9b to mitochondria.

Orf9b expression leads to a Tom70-dependent depletion of mitochondrial proteins in human cells

Next, we measured the relevance of Tom70 for the cellular proteome in cells cultured in respiring or fermenting growth conditions. To this end, we cultured the HEK293 WT or *Tom70* knock-down cells in galactose- or glucose-containing medium before cells were isolated and subjected to mass spectrometry (MS; Fig. 2 A and Fig. S2 A). Under both growth conditions, Tom70 was considerably depleted (to ∼20% of its endogenous levels). Strikingly, this resulted in considerable depletion of mitochondrial proteins only in respiring cells (Fig. 2 A). In glucose-grown and, hence, non-respiring cells, Tom70 depletion did not compromise mitochondrial biogenesis (Fig. S2 B). The depletion did not exclusively affect carrier proteins (including the atypical MTCH1 and MTCH2 carriers that reside in the outer membrane), but also proteins of the matrix, the intermembrane space, and the outer membrane. This is consistent with previous studies in yeast that showed the relevance of Tom70 to be not restricted to inner membrane proteins (Backes et al., 2021).

Furthermore, we tested the effect of Orf9b expression on the cellular proteome. Interestingly, we observed a rather general depletion of mitochondrial proteins again only in galactose-grown cells (Fig. 2, A and B), but not when cells were grown in glucose medium (Fig. 2 B and Fig. S2 B). The depletion was not as pronounced as in the Tom70-depleted cells (Fig. 2 B) but affected similar proteins (Fig. 2, C and D). Tom70 depletion and Orf9b expression shaped the mitochondrial proteome in a comparable way (Spearman rank correlation $\rho = 0.29$, $P = 1.2\ e^{-15}$), suggesting that Orf9b reduces the import-promoting function of Tom70. While most mitochondrial proteins were depleted in these cells, some were strongly increased, presumably as a response to Tom70 depletion; in particular, the epsilon subunit of the ATPase subunit ATP5E, a protein that was found to be strongly increased by stress response pathways and which therefore was used as a tumor marker in different types of cancers (Huang et al., 2019; Hurtado-López et al., 2015).

In summary, our results suggest that Orf9b expression leads to a characteristic footprint on the mitochondrial proteome that is similar to the one induced by Tom70 depletion. Apparently, the Orf9b protein of the SARS-CoV-2 virus has not only the potential to block the oligomer formation of MAVS on the mitochondria but is able to rewire the mitochondrial proteome on a large scale.

A yeast model with humanized Tom70 to elucidate the role of Orf9b in mitochondrial protein import

The observed strong effect of the Orf9b expression on the abundance of mitochondrial proteins might be directly caused by the competition of Orf9b with mitochondrial precursors for available Tom70 receptors. However, since Tom70 has many different functions in human cells including the induction of the mitochondrial antiviral signaling cascade (Kreimendahl and Rassow, 2020), more indirect effects of Orf9b expression cannot be excluded. We, therefore, developed an experimental system that is based on the baker's yeast *Saccharomyces cerevisiae*, the organism in which Tom70 function was most comprehensively analyzed. The overall structure of fungal and animal Tom70 is very similar (Chan et al., 2006; Young et al., 2003). However, the four amino acid residues of Tom70 that serve as binding sites for Orf9b (Gao et al., 2021) are not conserved from humans to yeast (Fig. 3 A and Fig. S3). A previous study reported that Orf9b localizes uniformly to the cytoplasm in yeast cells (Miserey-Lenkei et al., 2021), consistent with its inability to bind to yeast Tom70.

This inspired us to generate "humanized" yeast cells, in which the genes encoding the Tom70 (and Tom71) proteins were deleted and a chimeric protein consisting of parts of the yeast and human Tom70 was expressed (Fig. S4 A). This chimeric *Hs*Tom70 protein consists of the N-terminal outer membrane anchor of yeast Tom70 (residues 1–36) fused to the cytosolic domain of human Tom70 (residues 60–608). As indicated by the arrows in Fig. 3 B, the loss of Tom70 (and Tom71) caused a temperature-sensitive growth phenotype in yeast which was suppressed upon expression of either yeast Tom70 or the *Hs*Tom70 fusion protein. Mutations in critical residues in *Hs*Tom70 abolished this suppression (Fig. 3 B, control). Thus, the *Hs*Tom70 fusion protein can functionally replace the yeast Tom70 in vivo.

We further tested whether *Hs*Tom70 facilitates the import of Tom70-dependent proteins in yeast. To this end, we purified mitochondria from yeast strains that lacked Tom70 or contained either yeast Tom70 or *Hs*Tom70 and used these in in vitro import experiments. Therefore, we radiolabeled the ATP/ADP carrier of *Neurospora crassa* (Aac), a well-characterized model protein for Tom70 binding (Steger et al., 1990). Upon incubation with WT mitochondria, this carrier reached a protease-resistant location indicating its translocation across the outer membrane (Fig. 3 C). In contrast, mitochondria isolated from the *Δtom70* mutant did not efficiently take up the protein, unless either yeast Tom70 or the *Hs*Tom70 were expressed in these cells. Thus, *Hs*Tom70 can also replace the yeast Tom70 in vitro, allowing us to study the function of human Tom70 in our yeast model.

Orf9b binds to yeast mitochondria in an *Hs*Tom70-specific manner

Next, we expressed an HA-tagged Orf9b protein in these cells lacking the endogenous *TOM70* gene (for simplicity, we did not delete *TOM71*, which produces a minor isoform of the Tom70 receptor). Western blots indicated that only low amounts of Orf9b accumulated in the cells unless they contained the humanized *Hs*Tom70 protein (Fig. 4, A and B). The levels of Orf9b directly depended on the *Hs*Tom70 levels, as overexpression of *Hs*Tom70 from a stronger *GAL1* promoter resulted in higher Orf9b levels (Fig. 4 C). This resembles what we had observed in human cells, where Orf9b required its binding partner Tom70 to be protected against degradation.

The binding of Orf9b to *Hs*Tom70 was also confirmed by microscopy: expression of mScarlet-tagged Orf9b results in

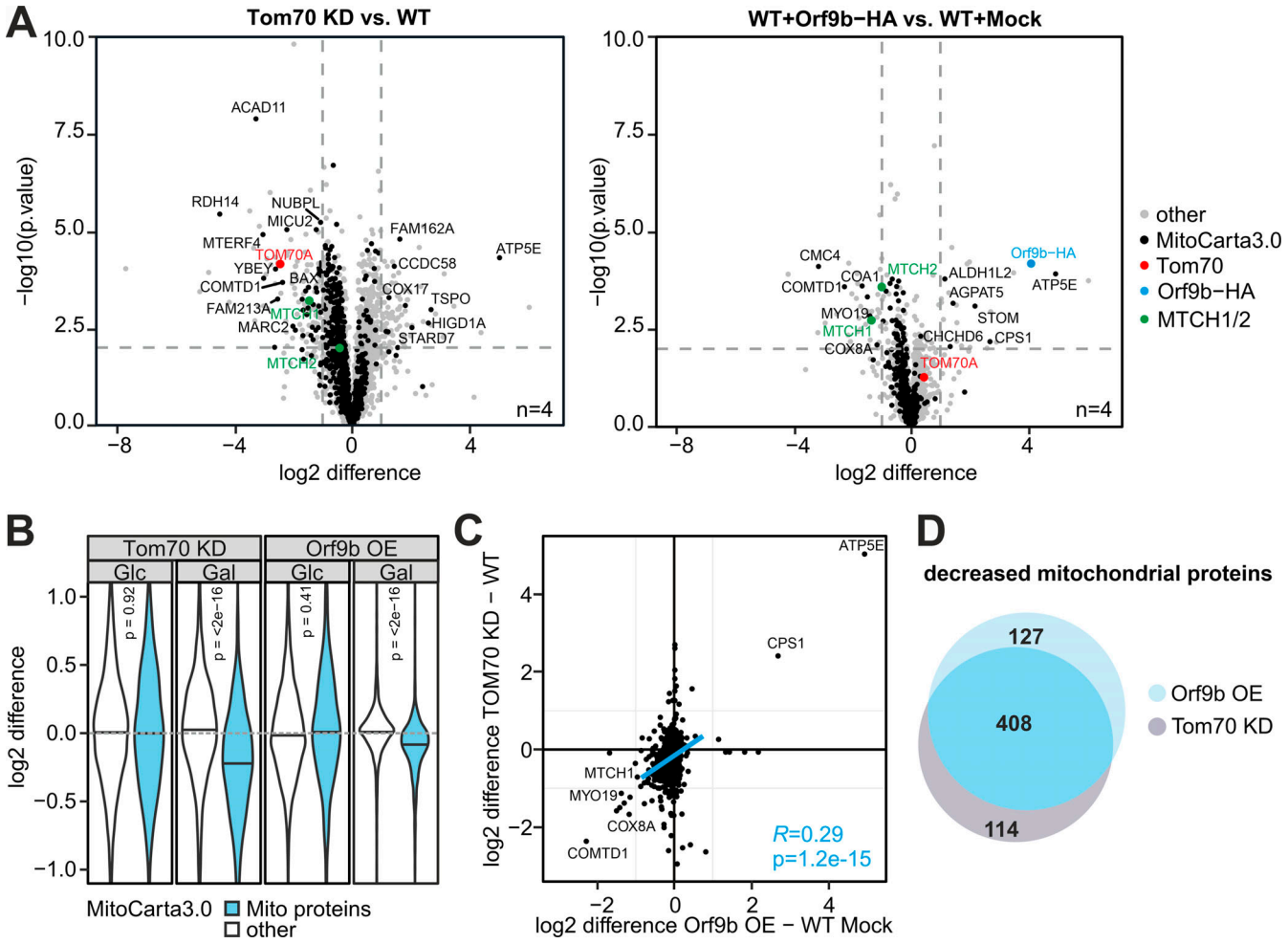

Figure 2. **Depletion of Tom70 or expression of Orf9b results in a moderate depletion of mitochondrial proteins. (A)** HEK293 cells were grown in galactose-containing medium. The proteomes of Tom70-depleted cells and control cells were compared by label-free MS of four independent biological replicates each (left panel). The right panel compares the proteomes of HEK293 cells that express Orf9b-HA for 4 d with that of a control. Mitochondrial proteins according to the MitoCarta 3.0 database (Rath et al., 2021) are highlighted in black. Fig. S2 shows the corresponding proteomes of cells grown in glucose-based medium for comparison. See Table S1 for the whole data set. Please note that mitochondrial proteins show the tendency to be less abundant in Orf9b-containing cells. **(B)** The difference in protein abundances between the presence or absence of Tom70 and/or Orf9b on galactose- or glucose-based medium is shown, based on the proteomics data. The significance of the shift in $\log_2$ fold changes was calculated using two-sided Wilcoxon rank sum tests between MitoCarta 3.0 and all other identified proteins. Note, that changes in the mitochondrial proteome can only be seen under respiring (galactose, Gal) but not fermenting (Glc, glucose) conditions. **(C)** Correlation plot for the fold changes of protein abundance shown in A (Tom70 knockdown [KD] vs. control against Orf9b overexpression [OE] vs. control). Please note the positive correlation of Tom70 depletion with Orf9b expression (Spearman rank correlation P = 1.2 e^{-15}) indicating that the loss of Tom70 and the expression of Orf9b lead to comparable changes of the cellular proteome. Proteins that were most reduced by Tom70 depletion such as COMTD1 and Cox8A were also strongly diminished upon expression of Orf9b. **(D)** Venn diagram demonstrating the overlap of mitochondrial (Rath et al., 2021) proteins decreased in both, Tom70 KD and Orf9b-HA overexpression; conditions based on the data shown in A ($\log_2$ difference <0).

colocalization with mitochondrial signal in cells that expressed *Hs*Tom70 (Fig. 4, D and E). However, Orf9b-mScarlet was not detectable in cells expressing the yeast Tom70, confirming the inability of the yeast homolog to recruit Orf9b to mitochondria. The role of the proteasome in Orf9b degradation was supported by the observation that cells with depleted proteasome levels (due to a CRISPRi-mediated depletion of the proteasome protein Pup2) showed considerably higher amounts of Orf9b, even if *Hs*Tom70 was not expressed (Fig. 4 F and Fig. S4 B).

In summary, we generated a humanized yeast model that allows it to recapitulate the effect of Orf9b on the Tom70-dependent import of proteins into mitochondria.

Orf9b expression depletes mitochondrial proteins in *Hs*Tom70-expressing yeast cells

Yeast cells neither have an antiviral stress response nor a homolog of MAVS. The *Hs*Tom70-expressing cells allowed us to analyze the effect of Orf9b expression in a strongly simplified system. To this end, we measured whole cell proteomes of *Δtom70* cells, lacking or expressing Orf9b and *Hs*Tom70. Principal component analysis (plot, Fig. 5 A) shows that Orf9b expression does not considerably influence the proteome in *Δtom70* cells unless the cells express *Hs*Tom70. This demonstrates the highly specific and *Hs*Tom70-dependent activity of Orf9b.

Tom70 is not essential for the biogenesis of mitochondrial proteins in vivo, but its absence leads to reduced levels of many

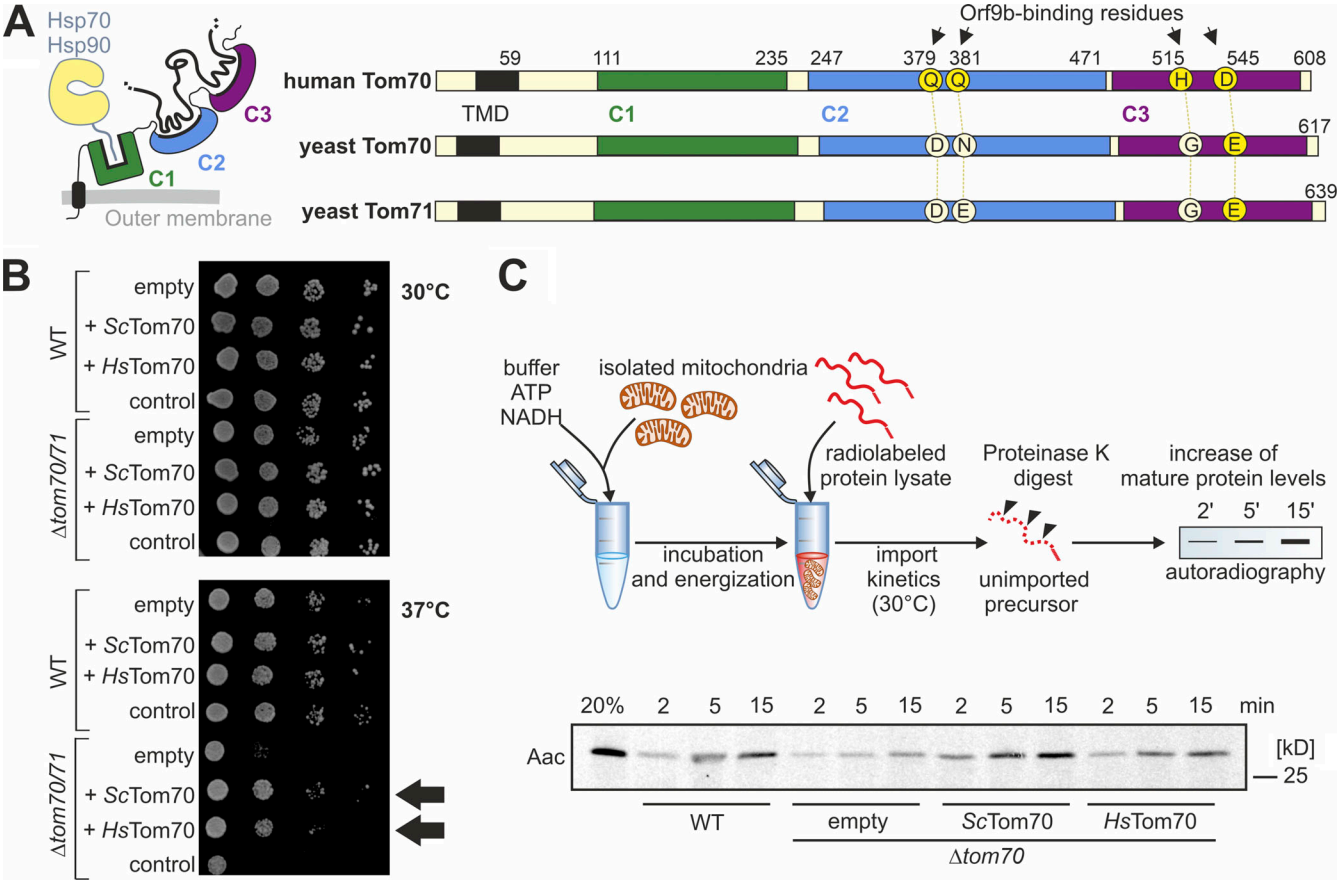

Figure 3. **The human Tom70 can functionally replace the Tom70 protein in the yeast *S. cerevisiae*. (A)** Schematic comparison of the Tom70 sequences of human and yeast homologs. The four human Tom70 residues that were reported to serve as direct contacts to Orf9b are indicated as well as the corresponding amino acid residues in the yeast homologs. See the alignment in Fig. S3 for details. TMD, transmembrane domain. **(B)** Expression of *Hs*Tom70 suppresses the growth defect of a Δ*tom70*/Δ*tom71* mutant in yeast comparable with the expression of the yeast Tom70 (*Sc*Tom70) protein (see arrows). For control, a non-functional *Hs*Tom70 variant was expressed in which all cysteine residues were replaced by serines. **(C)** Expression of *Hs*Tom70 facilitates the import of carrier proteins into isolated mitochondria. Mitochondria were isolated from Δ*tom70* cells carrying expression plasmids for yeast Tom70 or *Hs*Tom70, or empty plasmids for control. Radiolabeled ATP/ADP carrier (Aac) was incubated for the times indicated before non-imported proteins were removed by treatment with PK. Source data are available for this figure: SourceData F3.

mitochondrial proteins (Backes et al., 2021). The expression of the *Hs*Tom70 increased the levels of many mitochondrial proteins, again documenting its ability to take over the function of the yeast Tom70 at least to a certain extent (Fig. 5 B and Fig. S4 C). Expression of Orf9b-HA impaired the biogenesis of mitochondrial proteins in the *Hs*Tom70-expressing cells, albeit to a lesser extent than in human cells (Fig. 5 C). Again, we observed a rather good correlation (Spearman rank correlation R = 0.63, $P < 2.2\ e^{-16}$) of *Hs*Tom70-dependent and Orf9b-sensitive proteins (Fig. 5, D and E). In summary, the yeast-based model confirms that Orf9b has the potential to interfere with mitochondrial protein biogenesis in general. However, just as in human cells, the Orf9b effect was highly protein-specific, indicating that Orf9b does not just mute protein import into mitochondria in general, but rather modulates it in a specific, Tom70-dependent manner.

Orf9b impairs the import of Tom70-dependent mitochondrial precursor proteins

The posttranslational nature of the mitochondrial import system allows us to study the protein translocation process in vitro using radiolabeled precursor proteins. To avoid the loss of the Orf9b-HA protein from the mitochondria during the washing steps of the fractionation procedure during mitochondrial isolation, we used a system with semi-intact yeast cells which we recently optimized for the analysis of mitochondrial protein import (Hansen et al., 2018; Laborenz et al., 2019). This procedure employs yeast spheroplasts with enzymatically removed cell walls and permeabilized plasma membrane (Fig. 6 A). Matrix-targeted proteins were efficiently imported into mitochondria of spheroplasts, whereas the hydrophobic carrier proteins were not, presumably owing to their hydrophobicity (Fig. S4 D).

Many matrix-targeted precursors contain iMTS for Tom70 binding (Backes et al., 2018). We, therefore, tested the import efficiency of the iMTS-containing and Tom70-dependent protein Oxa1, and of Hsp60, which lacks iMTS sequences and does not bind to Tom70 (Backes et al., 2018). Hsp60 was efficiently imported into the mitochondria of semi-intact cells and reached a protease-resistant location, regardless of the presence or absence of Tom70 (Fig. 6 B). In contrast, the import of radiolabeled

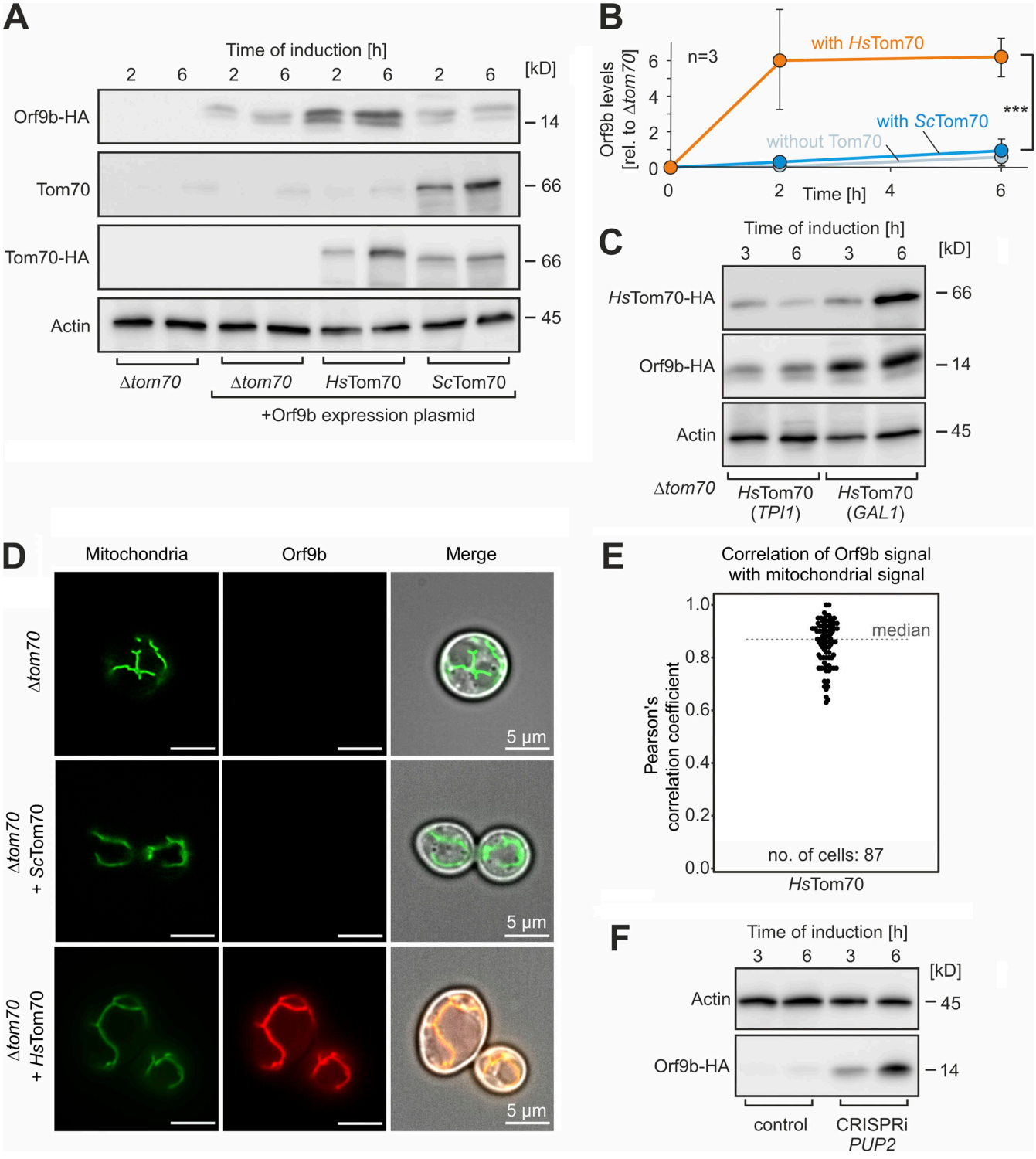

Figure 4. **Expression of *Hs*Tom70 stabilizes Orf9b in yeast cells. (A)** Orf9b-HA was expressed from a *GAL1*-driven promoter for 2 or 6 h in Δ*tom70* cells harboring plasmids for yeast Tom70 or *Hs*Tom70 expression or empty plasmids for control. Orf9b-HA, yeast Tom70, the HA-tagged *Sc*Tom70, and *Hs*Tom70 proteins as well as actin for control were detected by Western blotting. **(B)** The signals from A were quantified from three biological replicates. Significance was assessed using a two-sided unpaired Student's *t* test. The P values are indicated as asterisks. ***P ≤ 0.005. Please note that the accumulation of Orf9b in cells depends on the presence of its binding partner *Hs*Tom70, confirming the highly unstable nature of non-bound Orf9b. **(C)** Orf9b-HA was expressed in Δ*tom70* cells expressing *Hs*Tom70 from a *TPI1* or *GAL1* promoter. Please note, that the higher expression levels of *Hs*Tom70 of the *GAL1* sample also lead to higher levels of Orf9b in these cells. **(D)** Mitochondria-targeted Su9-mNeonGreen and Orf9b-mScarlet were constitutively expressed in the indicated strains and visualized by fluorescence microscopy. Please note that Orf9b-mScarlet was only detectable in cells if *Hs*Tom70 was present. Scale bar = 5 µm. **(E)** Quantitative assessment of the colocalization of Orf9b-mScarlet and Su9-mNeonGreen. In cells that did not express *Hs*Tom70, Orf9b-mScarlet was not detectable and therefore correlations could not be measured. **(F)** Orf9b-HA expressing cells were transformed with a plasmid for the CRISPRi-mediated depletion of the proteasomal protein Pup2 or an empty vector for control. The levels of Orf9b-HA and Act1 for control were analyzed by Western blotting. Source data are available for this figure: SourceData F4.

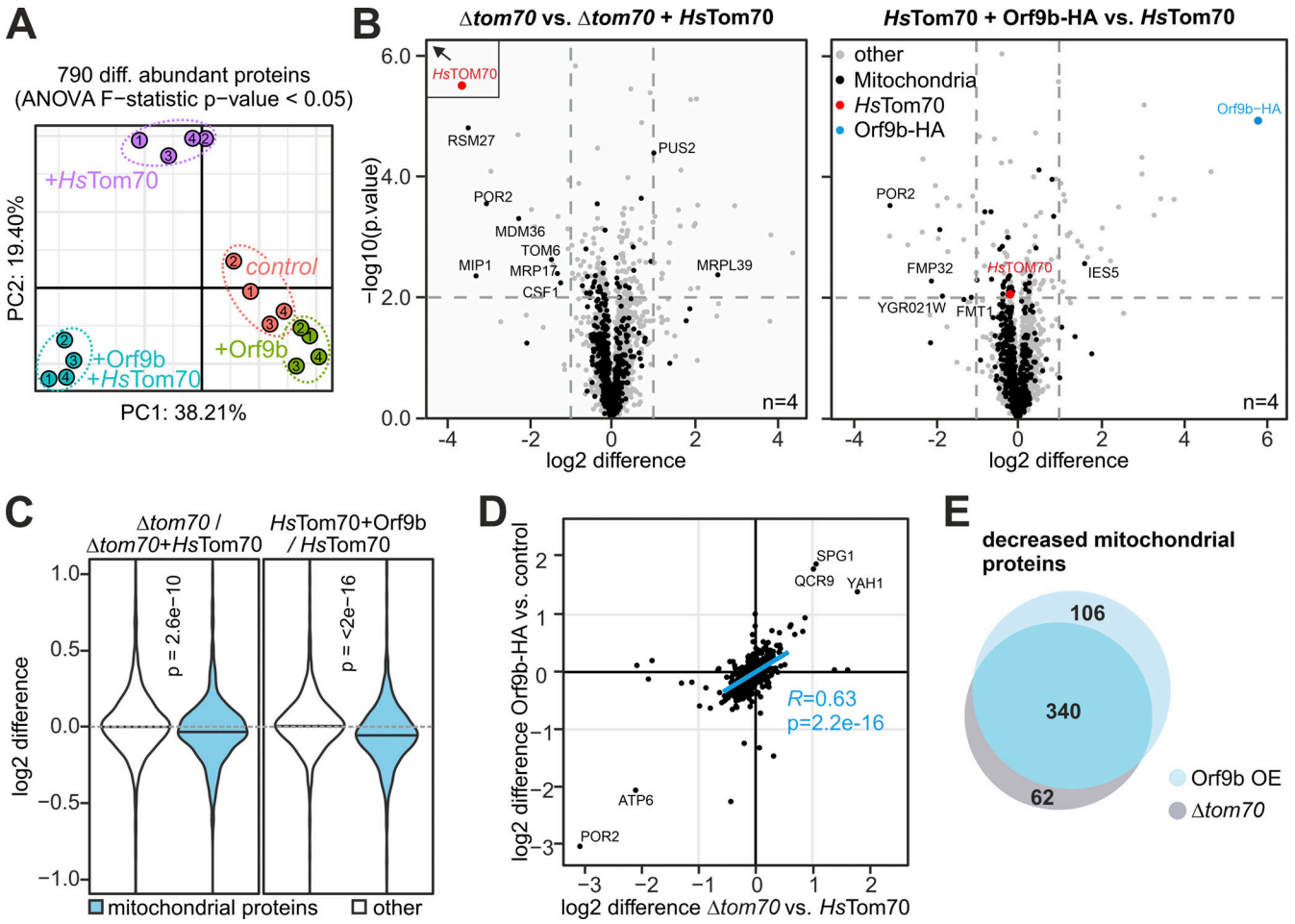

Figure 5. **Expression of Orf9b depletes mitochondrial proteins in *Hs*Tom70-containing cells. (A)** Cells of the Δ*tom70* mutant were transformed with plasmids for the expression of *Hs*Tom70 and Orf9b-HA. Cells were grown in SLac medium to mid-log phase. Galactose (0.5%) was added to induce Orf9b expression for 16 h before cells were harvested. The proteomes of whole cell extracts of four biological replicates each were analyzed by MS. Principal component (PC) analysis shows that Orf9b expression has a strong effect, however, only in *Hs*Tom70-expressing cells. **(B)** Volcano plots show that expression of *Hs*Tom70 increases the levels of many mitochondrial proteins (left panel) and Orf9b expression prevents this *Hs*Tom70-dependent accumulation. The position of *Hs*Tom70 is outside of the shown graph; please see Fig. S4 C for a version in which the position of *Hs*Tom70 is shown to scale. **(C)** The $\log_2$ fold changes in protein abundance of mitochondrial (Morgenstern et al., 2017) and non-mitochondrial proteins were plotted based on the data shown in B. The P values were derived as described for Fig. 2 B. **(D)** Correlation plot for the enrichment scores of the proteomes shown in B. Please note that proteins that are increased by the expression of *Hs*Tom70 in Δ*tom70* cells correlate with those that are depleted by Orf9b expression ($P = 2.2\ e^{-16}$). Proteins that strongly depend on *Hs*Tom70 are Por2 and Mrp17. **(E)** Venn diagram showing the overlap of *Hs*Tom70-dependent and Orf9b-sensitive mitochondrial proteins.

Oxa1 into the mitochondria was strongly improved by the presence of *Hs*Tom70, an effect that was compromised if the yeast cells expressed Orf9b-HA (Fig. 6, B and C). Likewise, Orf9b inhibited the import of the multispanning inner membrane proteins Tim17 and Oac1 into *Hs*Tom70-containing mitochondria (Fig. 6, D and E).

In summary, our in vitro model confirms the Orf9b-mediated inhibition of human Tom70 and the potential of this viral protein to modulate the import of proteins into mitochondria.

Orf9b expression reduces the mitochondrial volume in HsTom70-expressing yeast cells

Next, we measured the mitochondrial volume of yeast cells expressing a mitochondria-targeted mNeonGreen protein (Böttinger et al., 2012; Fig. 7 A). From z-stacks of microscopic images, the volumes of cells as well as of mitochondria were quantified using a semiautomated pipeline (Fig. 7 B). This revealed that the mitochondrial volume of Δ*tom70* is considerably increased by expression of *Hs*Tom70. This again supports the idea that Tom70 (and *Hs*Tom70) promotes mitochondrial biogenesis. Expression of Orf9b represses the function of *Hs*Tom70 and the mitochondrial volume remains as small as it is in Tom70-deficient cells (Fig. 7 C). Thus, in humanized yeast cells, Orf9b expression is sufficient to considerably repress mitochondrial biogenesis.

Discussion

Despite its limited size of just about 30 kb, the coding capacity of the SARS-CoV-2 virus is surprisingly large. By strategies such as overlapping genes, frameshifting events, and the synthesis of a long multiprotein precursor that is proteolytically cleaved into

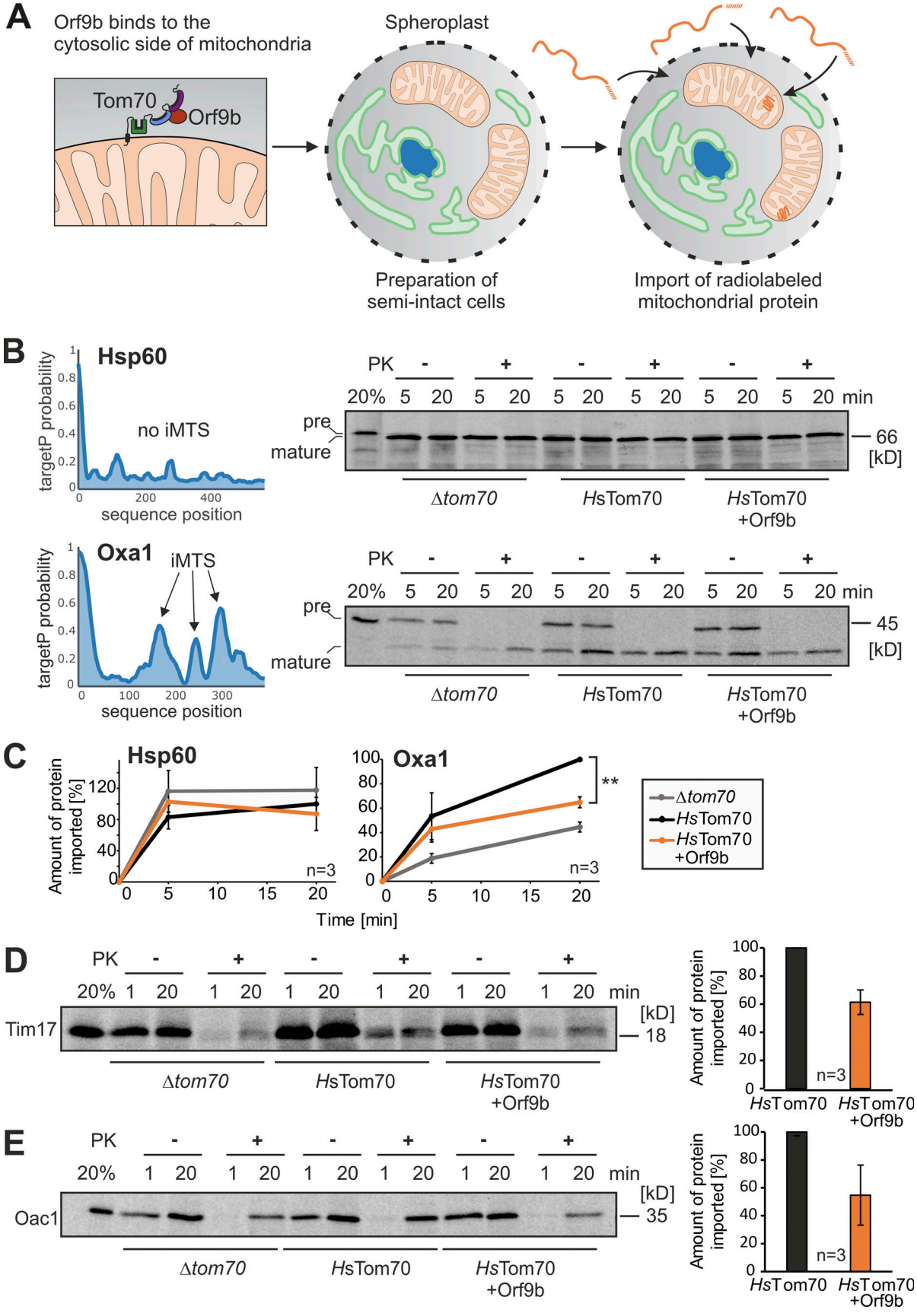

Figure 6. **Orf9b inhibits the import of the Tom70-dependent protein Oxa1. (A)** Schematic representation of the in vitro import assay with semi-intact yeast cells. **(B)** Radiolabeled precursor of Hsp60 and Oxa1 were incubated with semi-intact cells of the indicated strains for 5 and 20 min at 30°C. Non-

imported proteins were removed by treatment with PK for 30 min on ice before samples were analyzed by SDS-PAGE and autoradiography. TargetP prediction scores were calculated for Hsp60 and Oxa1 as described previously (Backes et al., 2018; Schneider et al., 2021). Precursor and mature species were indicated by pre and mature, respectively. **(C)** Quantification of the relative amounts of imported proteins of three independent biological experiments. For quantification, the signals in the protease-treated samples were measured and shown in comparison with the longest time point of the *Hs*Tom70 control, which was set as 100%. Significance was assessed using a two-sided unpaired Student's *t* test. The P values are indicated as asterisks; **P ≤ 0.01. **(D and E)** Radiolabeled Tim17 and Oac1 were incubated with semi-intact cells and further treated as described in B. Tim17 and Oac1 are multi-spanning inner membrane proteins. For quantification, the signals after 20 min of import in cells lacking or containing Orf9b were compared from three independent biological replicates. Source data are available for this figure: SourceData F6.

16 nonstructural proteins, the virus produces an impressively complex translation landscape. Among the many viral proteins, Orf9b is the third most abundant one (only the nucleocapsid and the membrane protein M reach higher cellular levels), indicating a very important function of this protein (Finkel et al., 2021). Our observations confirm that Orf9b binds specifically to Tom70 on the mitochondrial surface; non-bound Orf9b is rapidly degraded by the proteasome, suggesting that the high levels found in virus-infected cells indeed reflect Tom70-bound Orf9b. This high abundance is compatible with the role of Orf9b as a competitive inhibitor of Tom70, which likewise is a rather abundant protein (Morgenstern et al., 2021).

Many of these viral gene products tailor cellular processes to the virus' needs. For example, the ORF8 protein of SARS-CoV-2 serves as a histone mimic that prevents modification of the histone H3, thereby suppressing the cellular ability to respond to the virus infection by epigenetic regulation (Kee et al., 2022). Viruses also target the translocation of proteins into cellular compartments, such as mitochondria, the ER, and the nucleus. The proteins of the ER-associated degradation pathway even were initially discovered in cytomegalovirus-infected cells by the specific targeting of viral proteins (Wiertz et al., 1996). The UL37 protein of human cytomegalovirus is a well-studied modulator of the mitochondrial protein import system. It binds to the mitochondrial import receptor Tom20, thereby jeopardizing the proapoptotic function of Bax (Goldmacher et al., 1999; Williamson and Colberg-Poley, 2010). The TOM receptors Tom20 and Tom70 are functionally overlapping (Ramage et al., 1993), and inhibition of one of these receptors will therefore not block protein translocation completely but rather modulate it. In the case of cytomegaloviruses, this UL37-mediated Tom20 modulation disables host cells to undergo Bax-mediated apoptosis while protein import and mitochondrial function are not generally compromised.

We observed that Orf9b expression caused a considerable modulation of the mitochondrial proteome, thereby depleting many mitochondrial proteins (Fig. 7 D). Some proteins were found to be particularly sensitive to Orf9b expression or Tom70 depletion, such as the outer membrane proteins MTCH1 and MTCH2. Whereas other members of the carrier family reside in the inner membrane, MTCH1 and MTCH2 are outer membrane proteins where they serve as insertases for mitochondrial tail-anchored proteins (Guna et al., 2022). It will be exciting to test in the future whether Orf9b expression influences the biogenesis of tail-anchored proteins.

Despite the depletion of mitochondrial proteins, Orf9b-expressing HEK293 cells were still able to respire and hence grow on galactose. Changes in the mitochondrial proteome of SARS-CoV-2–infected cells and mitochondrial dysfunction were reported in several proteomic studies (Bhowal et al., 2022; Bojkova et al., 2020; Chang et al., 2022; Denaro et al., 2022; Gibellini et al., 2020; Shi et al., 2014; Stukalov et al., 2021; Surendran et al., 2022). It seems likely that the Orf9b-mediated inhibition of Tom70 contributes to this effect. The fact that evolved virus variants such as Delta and Omicron show an increased Orf9b expression suggests that the improved targeting of the mitochondrial import machinery serves as one mechanism of coronaviruses to maximize their propagation (Hossain et al., 2022; Thorne et al., 2022). Since one infected human cell was estimated to produce between 100,000 and 1,000,000 virions (Sender et al., 2021), which is higher than the copy number of Tom70 (37–58,000 per cell; Morgenstern et al., 2021), the levels of Orf9b should be high enough to saturate all Tom70 binding sites.

The function of Tom70 is highly complex (Kreimendahl and Rassow, 2020). In yeast cells, in addition to its role in protein import, Tom70 forms ER–mitochondria contact sites by binding to the ER proteins Lam6/Ltc1 and Djp1 (Elbaz-Alon et al., 2015; Hansen et al., 2018; Murley et al., 2015). These contacts presumably help to exchange lipids between intracellular membranes (Murley et al., 2017). In human cells, the role of Tom70 in contact site formation is less well understood; however, homologs of Lam6/Ltc1 are conserved in eukaryotes and it is well possible that coronaviruses use Orf9b to modulate such Tom70-mediated ER–mitochondria contact sites.

Moreover, in human cells, Tom70 serves as a central player in antiviral defense reactions (Jacobs and Coyne, 2013; Liu et al., 2010; McWhirter et al., 2005; Shi et al., 2015). The humanized yeast cells used in this study allowed us to investigate the effect of Orf9b on Tom70 in a model lacking any antiviral response. The results of this in vivo reconstitution demonstrated the capacity of Orf9b to interfere with mitochondrial protein import in vivo and in vitro and the strong variability of different mitochondrial precursor proteins with respect to their specific Orf9b sensitivity (Fig. 7 D). Again, this suggests that Orf9b does not mute mitochondrial biogenesis in general but rather modulates it. Despite the reduced volume of mitochondria observed in Orf9b-expressing cells, we did not observe a reduced growth or fitness of the Orf9b-expressing *Hs*Tom70 cells, contrary to other mutants of the import system, which often are severely compromised. This yeast-based system now allows better exploration of the specific relevance of Tom70 but also promises to serve as an attractive model to screen for Orf9b inhibitors that maintain Tom70 activity in the presence of Orf9b.

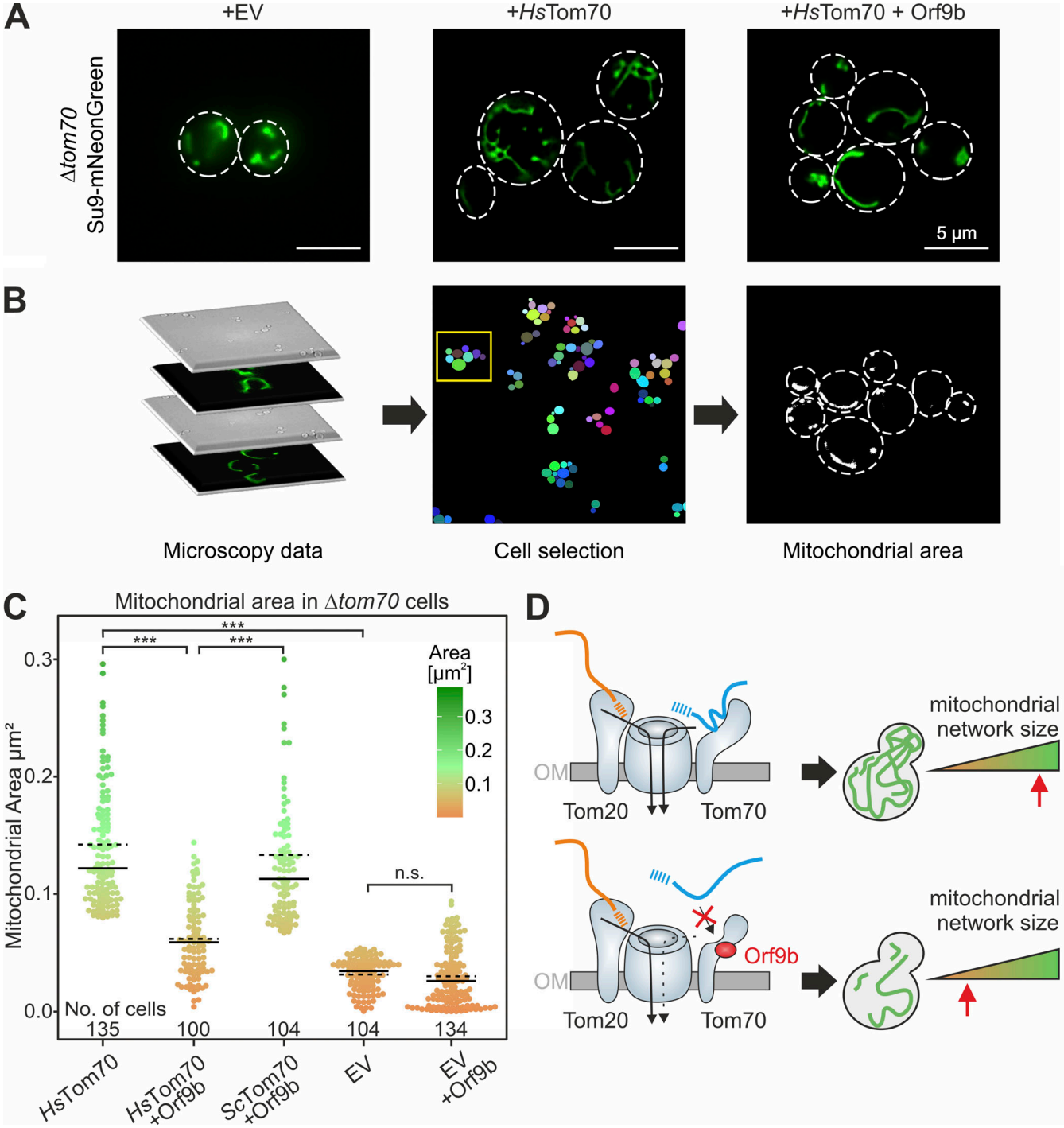

Figure 7. **Expression of Orf9b reduces the volume of mitochondria in *Hs*Tom70-expressing cells. (A)** The indicated cells were transformed with plasmids for expression of mitochondria-targeted mNeonGreen. Cells were grown in SLac medium to mid-log phase, Orf9b expression was induced with galactose for 6 h, and mitochondria were visualized by microscopy. EV, empty vector. **(B)** From the images analyzed, cells were selected and the fluorescent areas within the cells were quantified by ImageJ/Fiji analyze particles algorithm. See Materials and methods for details. **(C)** Quantification of the mitochondrial areas from the cells indicated using the workflow sketched in B. Solid lines represent the median, dotted lines represent the mean. Please note that expression of *Hs*Tom70 increases the mitochondrial area, but this effect is prevented by Orf9b expression. See Materials and methods for statistical analysis. The number of cells (technical replicates) are indicated in the figure. The P values are indicated as asterisks. ***P ≤ 0.001. **(D)** Schematic representation of the Orf9b-induced inhibition of Tom70-dependent protein import into mitochondria. By its interference with Tom70 function, Orf9b diminishes the mitochondrial volume, explaining the mitochondrial dysfunction observed in cells infected by the SARS-CoV-2 virus. OM, outer membrane. Source data are available for this figure: SourceData F7.

Materials and methods

Yeast strains and plasmids

All yeast strains used in this study are based on the WT strains W303 (MATα *leu2 trp1 can1 ura3 ade2 his3*) or YPH499 (MATa *ura3 lys2 ade2 trp1 his3 leu2; ARG4::kanMX4*; Sikorski and Hieter, 1989). To delete *TOM70* or *TOM71*, the genes were chromosomally replaced by a kanMX4 or natNT2 cassette using pFA6α-kanMX4/natNT2 as a template.

To generate a humanized version of Tom70 for the expression in yeast cells (denoted as *Hs*Tom70 in this study), the coding regions for the cytosolic domain (residues 60–617) were amplified from a plasmid (ordered from GenScript) containing the yeast codon-optimized sequence of *H.s.* Tom70 (*H.s.* Tom70-cyt-F: 5′-GGG**GGATCC**CGGCAGCAACGGCG-3′; *H.s.* Tom70-cyt-R: 5′-GGG**CCCGGG**TAATGTTGGTGGTTTTAATC-3′). Bold letters in the primer sequences show the cutting sites of enzymes used for cloning. The product was ligated into a pYX142 (*TPI1* promoter) plasmid encoding the transmembrane domain of *S.c.* Tom70 (residues 1–36; *S.c.* Tom70-TMD-F: 5′-GGG**GAATTC**ATGAAG AGCTTCATTACAAGG-3′, *S.c.* Tom70-TMD-R: 5′-GGG**CCCGGG** CATTAAACCCTGTTCG-3′). *BamH*I and *Xma*I restriction sites were used resulting in a fusion product of *H.s.* Tom70 cytosolic domain and *S.c.* transmembrane domain. This fusion gene was also ligated into a pYX233 plasmid (*GAL1* promoter) using *EcoRI* and *XhoI* restriction sites. A mutated version of the *H.s.* Tom70 cytosolic domain was used as a negative control in Fig. 3. For this construct,12 cysteine residues were mutated to serine. To generate the Orf9b expression plasmid, the coding sequence was amplified from a plasmid (ordered from GenScript) encoding the yeast codon-optimized sequence of SARS-CoV-2 Orf9b (Table S2). The product was ligated into a pYX123 plasmid downstream of the *GAL1* promoter and in front of an HA tag using the restriction sites *Eco*RI and *HindIII* employing a Gibson assembly protocol (Orf9b-HA-F: 5′-GGAGAAAAAACCCCGGATCGATGG ACCCAAAAATAAGTGAAATG-3′; Orf9b-HA-R: 5′-TACTAACCA TTGCGTAGTCAGGCACATC-3′). For fluorescence microscopy, Orf9b was C-terminally tagged with mScarletI. The Orf9b coding sequence was amplified from pYX123-Orf9b and assembled via Gibson assembly with mScarletI (amplified from #118457; Addgene) into pYX123 using *Eco*RI and *Hind*III restriction sites (Orf9b-mScarletI-F: 5′-TGACTACGCAATGGTTAGTAAAGGTGA AG-3′; Orf9b-mScarletI-R: 5′-GATACCCGGGTCGACGCGTAT TATTTATACAATTCATCCATTCC-3′). For genomic integration of Su9-mNeonGreen, mNeonGreen was amplified from #125703; Addgene (Botman et al., 2019) and cloned via Gibson assembly into pRS306 after the mitochondrial targeting sequence of ATP-synthase subunit 9 using *Spe*I and *Eco*RI. To generate a *PUP2* knock-down strain, we employed a single plasmid CRISPRi system. The *PUP2* gRNA was assembled by annealing two oligonucleotides (*PUP2*-Cri1-F: 5′-AGGGCTCTCTTGTCCAATTTC CT-3′; *PUP2*-Cri1-R: 5′-AACAGGAAATTGGACAAGAGAGC-3′) to form a double-stranded sticky end fragment. pKR366 was digested with BspQI and the fragment was inserted using T4-ligase (Backes et al., 2021; Smith et al., 2016). All plasmids were verified by sequencing.

All yeast plasmids used in this study are listed in Table S2. Empty plasmids were used for control. For yeast transformation, the lithium acetate method was used (Gietz et al., 1992). Yeast cells carrying plasmids were grown in a minimal synthetic medium containing 0.67% (wt/vol) yeast nitrogen base and 2% of glucose, galactose, or lactate (SLac), as indicated. For plates, 2% of agar was added to the medium. To induce protein expression from the *GAL1* promoter, 0.5% of galactose was added to the yeast cultures.

Human cell lines and plasmids

For plasmids used for human cells, see Table S2. All cell lines were cultured in Dulbecco's modified Eagle's medium (DMEM) complete containing 4.5 g liter^{-1} glucose, 8% fetal bovine serum, and 500 µg ml^{-1} penicillin/streptomycin at 37°C under 5% CO_2. For the generation of stable, doxycycline-inducible cell lines, the HEK293 cell line-based Flp-In T-REx-293 cell line in a WT and Tom70 knock-down background was used with the Flp-In T-REx system (Invitrogen). For expression of Orf9b-HA, the primers Orf9b-HA-F: 5′-CGCGGTACCGCCACCATGGACCC-3′ and Orf9b-HA-R: 5′-GCGGCGGCCGCTTATGCATAATCAGGTACATCATAA GGATAGGACCCCTTTACGGTTACTACC-3′ were used. Positive clones were selected with DMEM complete medium containing 100 µg ml^{-1} hygromycin and 10 µg ml^{-1} blasticidin. The expression of stable cell lines was induced for at least 16 h with 1 mg ml^{-1} doxycycline. For experiments carried out in galactose medium, cells were cultivated in DMEM complete containing 4.5 g liter^{-1} galactose, 8% fetal bovine serum, 500 µg ml^{-1} penicillin/streptomycin, MEM non-essential amino acids 100× (#M7145; Sigma-Aldrich), and 1 mM sodium pyruvate (#S8636; Sigma-Aldrich) at 37°C under 5% CO_2 for at least 2 wk before the experiment.

CRISPR-Cas9-based generation of *Tom70* HEK293 knock-down cell line

For the generation of *Tom70* knock-down cells, gRNA sequences targeting human *Tom70* were cloned into the pSpCas9(BB)-2A-GFP (PX458) vector, which was a gift from Feng Zhang (plasmid # 48138; Addgene; Ran et al., 2013). The guide RNA sequence (TOMM70_Guide3_Exon1_fw: 5′-CACC-G-TGTACCGAGCTC CGGGAGTGGGG-3′) was chosen to generate the knockdown. HEK Flp-In T-REx-293 cells were transfected with the plasmid using polyethyleneimine (Thermo Fisher Scientific). After 24 h, GFP-positive cells were collected via FACS, and single-cell clones were seeded onto 96-well plates (1 cell/well). Clonal cell lines were screened for Tom70 protein expression by Western blotting.

Drop dilution assay

For drop dilution assays, respective yeast strains were grown in yeast synthetic media to mid-log phase. After harvesting 0.5 OD_{600} of cells and washing with sterile water, a 1:10 dilution series was prepared. 3 µl of each dilution was dropped on agar plates containing full or synthetic media. Pictures of the plates were taken after different days of incubation at 30°C or 37°C.

Preparation of whole-cell lysates from yeast cells

For the preparation of whole-cell lysates, four OD_{600} yeast cells were harvested and washed with sterile water. Pellets were

resuspended in 40 µl Laemmli buffer (2% SDS, 10% glycerol, 50 mM dithiothreitol [DTT], 0.02% bromophenol blue, 60 mM Tris/HCl, pH 6.8) containing 50 mM DTT and heated at 96°C for 3 min. Cells were lysed using glass beads of 1 mm in diameter and vortexed for 1 min. 80 µl Laemmli buffer was added and samples were stored at −20°C until visualization by Western blotting.

Preparation of whole-cell lysates of human cells

To analyze steady-state protein levels, cells were washed once with ice-cold PBS and harvested in Laemmli buffer (2% SDS, 60 mM Tris-HCl, pH 6.8, 10% glycerol, and 0.0025% bromophenol blue) containing 50 mM DTT. Lysis was performed by boiling for 5 min at 96°C. To inhibit the proteasome, cells were treated with 1 µM MG132 (Sigma-Aldrich) or with DMSO as control for 16 h at 37°C before lysis. Protein samples were analyzed by SDS-PAGE and immunoblotting. The addition of 2,2,2-trichloroethanol (TCE) into the SDS-PAGE gel allowed for the visualization of migrated proteins and as a loading control.

Isolation of mitochondria from yeast cells

To isolate crude mitochondria, yeast strains were cultivated in synthetic galactose media to mid-log phase and harvested by centrifugation (5 min, 3,000 *g*). After washing the pellets with water and centrifugation (5 min, 3,000 *g*), the weight of the cell pellet was determined. Pellets were resuspended in 2 ml/g wet weight in MP1 (100 mM Tris, 10 mM DTT), incubated for 10 min at 30°C, and centrifuged again (5 min, 3,000 *g*). Pellets were washed with 1.2 M sorbitol and centrifuged (5 min, 3,000 *g*) before resuspending in 6.7 ml/g wet weight in MP2 (20 mM KPi buffer, pH 7.4, 1.2 M sorbitol, 3 mg/g wet weight zymolyase from Seikagaku Biobusiness) and incubated at 30°C for 60 min. The following steps were conducted on ice. After centrifugation (5 min, 2,800 *g*), pellets were resuspended in 13.4 ml/g wet weight in homogenization buffer (10 mM Tris, pH 7.4, 1 mM EDTA, 0.2% BSA, 1 mM PMSF, 0.6 M sorbitol), and a cooled glass potter was used to homogenize the sample with 10 strokes. After homogenization, the extract was centrifuged three times (5 min, 2,800 *g*) while always keeping the mitochondria-containing supernatant. To pellet mitochondria, samples were centrifuged for 12 min at 17,500 *g*. Pellets were resuspended in SH buffer (0.6 M sorbitol, 20 mM Hepes, pH 7.4). The concentration of the purified mitochondria was adjusted to 10 mg/ml protein. Aliquots were snap-frozen in liquid nitrogen and stored at −80°C.

Import of radiolabeled precursor proteins into mitochondria

To prepare radiolabeled (^{35}S-methionine) proteins for import experiments, the TNT Quick Coupled Transcription/Translation Kit from Promega was used according to the instructions of the manufacturer. To determine the ability of proteins to be imported into mitochondria expressing *Hs*Tom70, in vitro import assays were conducted. Mitochondria were resuspended in a mixture of import buffer (500 mM sorbitol, 50 mM Hepes, pH 7.4, 80 mM KCl, 10 mM $Mg(OAc)_2$, 2 mM KPi) with 2 mM ATP and 2 mM NADH to energize them for 10 min at 30°C. The import reaction was started by the addition of the radiolabeled lysate (1% final volume). Import was stopped after 2, 5, and 15 min by transferring the mitochondria into cold SH buffer (0.6 M sorbitol, 20 mM Hepes, pH 7.4). The remaining precursors outside of the mitochondria were removed by proteinase K (PK) treatment for 30 min. Moreover, 2 mM PMSF was added to stop protein degradation by inhibiting PK. After centrifugation (15 min, 25,000 *g*, 4°C), the supernatant was removed. Pellets were resuspended in SH buffer containing 150 mM KCl and 2 mM PMSF (SH-KCl) and centrifuged again (15 min, 25,000 *g*, 4°C). Pellets were then lysed in Laemmli buffer (2% SDS, 10% glycerol, 50 mM DTT, 0.02% bromophenol blue, 60 mM Tris/HCl, pH 6.8) and heated to 96°C for 3 min. Samples were run on a 16% SDS gel, blotted onto a nitrocellulose membrane, and visualized with autoradiography.

Preparation of semi-intact cells

The protocol for the preparation of semi-intact cells was adapted from Schlenstedt et al. (1993). The following buffers were used: SP1 (10 mM DTT, 100 mM Tris, pH not adjusted); SP2 (0.6 M sorbitol, 1× yeast extract and peptone, 0.2% glucose, 50 mM KPi, pH 7.4, 3 mg/g wet weight zymolyase); SP3 (1× yeast extract and peptone, 1% glucose, 0.7 M sorbitol); and permeabilization buffer (20 mM Hepes, pH 6.8, 150 mM KOAc, 2 mM Mg-acetate, 0.4 M sorbitol). Precultures were grown in 250 ml galactose or SLac with 0.5% galactose at 30°C. Cells were harvested (700 g, 7 min, RT) in the exponential phase. The cell pellet was resuspended in 25 ml SP1 buffer and incubated for 10 min at 30°C shaking. After centrifugation (1,000 *g*, 5 min, RT), the pellet was resuspended in 6 ml SP2 buffer and incubated at 30°C for maximum 60 min. The spheroplast formation was monitored every 15 min. Spheroplasts were collected and resuspended in 40 ml of SP3 buffer and incubated for 20 min at 30°C shaking. After centrifugation (1,000 *g*, 5 min, 4°C), spheroplasts were washed two times with 20 ml of ice-cold permeabilization buffer. The pellet was resuspended in 1 ml permeabilization buffer containing 0.5 mM EGTA and 100 µl aliquots were slowly frozen over liquid nitrogen for 30 min.

Import into semi-intact cells

Semi-intact cells were thawed on ice and the OD_{600} was measured in 1.2 M sorbitol. Semi-intact cells of an OD_{600} 0.2 were used per reaction. Semi-intact cells were added to a mixture of 2 mM ATP, 2 mM NADH, 5 mM creatine phosphate, 100 µg/ml creatine phosphatase, and B88 buffer (20 mM Hepes, pH 6.8, 150 mM KOAc, 5 mM Mg(OAc)2, 250 mM sorbitol). The radiolabeled lysate was added and the mixture was incubated for 10 min on ice to allow the cells to take up the lysate. Afterward, the suspensions were incubated at 30°C. For kinetics, samples were taken after 5 and 20 min. The import reaction was stopped in a 1:10 dilution of ice-cold B88 buffer supplemented with 20 mM carbonyl cyanide m-chlorophenyl hydrazine. In addition, the samples were treated with or without 100 µg/ml PK for 30 min on ice. The protein digestion was stopped by the addition of 200 mM PMSF. Semi-intact cells were centrifuged (4,000 *g*, 5 min, 4°C), washed again with B88 and 200 mM PMSF, and centrifuged for 10 min at 16,000 *g* and 4°C. Finally, the pellet was resuspended in reducing Laemmli buffer (2% SDS, 10% glycerol, 50 mM DTT, 0.02% bromophenol blue, and 60 mM Tris/HCl, pH

6.8). Samples were run on a 16% SDS gel, blotted onto a nitrocellulose membrane, and visualized with autoradiography.

Isolation of mitochondria from human cells

For isolation of crude mitochondria from human cells, HEK Flp-In T-REx-293 WT cells were cultured in DMEM supplemented with glucose. Expression of Orf9b-HA was induced with 1 µg/ml doxycycline for the indicated time prior to lysis. Isolation of crude mitochondria was performed as described before (Murschall et al., 2021). In brief, cells were seeded onto 15-cm dishes and lysed after reaching confluence. Cells were washed with PBS, scratched off, and transferred into a 15-ml reaction tube. After centrifugation for 5 min at 500 *g*, cell pellets were resuspended in 5 ml buffer M (220 mM mannitol, 70 mM sucrose, 5 mM Hepes-KOH, pH 7.4, 1 mM EGTA-KOH, pH 7.4) containing 1 × Complete TM Protease Inhibitor Cocktail. Cells were homogenized using a potter homogenizer at 1,000 rpm for 15 strokes before pelleting at 600 *g* for 5 min. Crude mitochondria from the supernatant were collected by centrifugation at 8,000 *g* for 10 min and washed with 2 ml cold buffer M. Finally, crude mitochondria were pelleted at 6,000 *g* for 10 min and resuspended in 400 µl buffer M. The protein amount was determined using the BCA Reagent ROTI Quant Assay according to the manufacturer's instructions. Mitochondria were lysed in Laemmli buffer (2% SDS, 10% glycerol, 0.02% bromophenol blue, and 60 mM Tris/HCl, pH 6.8), boiled for 5 min at 96°C, and analyzed via SDS-PAGE and Western blot.

Antibodies

The antibodies against Act1, Tom70, and Tom22 were raised in rabbits using recombinant purified proteins. The secondary antibody was obtained from Bio-Rad (Goat Anti-Rabbit IgG [H+L]-HRP Conjugate #172-1019) or ImmunoReagents Inc. (Goat anti-Rabbit IgG [H&L]—Affinity Pure, HRP Conjugate, #GtxRb-003-DHRPX, Goat anti-Mouse IgG [H&L]—Affinity Pure, HRP Conjugate, #GtxMu-003-DHRPX). The horseradish-peroxidase coupled HA antibody was purchased from Roche (Anti-HA-Peroxidase, High Affinity [3F10], #12 013 819 001). The HA-tag antibody used in immunofluorescence and Western blot assays was purchased from Sigma-Aldrich (Anti-HA-Tag antibody produced in rabbits, #SAB4300603). The Tom70 antibody was purchased from Sigma-Aldrich (Anti-TOMM70 antibody produced in rabbit, #HPA048020). For analysis of isolated human mitochondria, the following additional antibodies were used: Anti-Hsp90 (#4874S; Cell Signaling Technology), Anti-PDH (#sc-377092; Santa Cruz), Anti-MTCH2 (#16888-1-AP; Proteintech), Anti-Hsp70 (#4872S; Cell Signaling Technology), Anti-GAPDH (#sc-32233; Santa Cruz), Anti-AK2 (rabbit, self-made). Antibodies were diluted in 5% (wt/vol) nonfat dry milk in 1× TBS buffer in a 1:1,000 dilution, except for: Anti-HA-Peroxidase 1:500, Anti-Rabbit 1:10,000, and Anti-Mouse 1:5,000.

Sample preparation and mass spectrometric identification of proteins in yeast

For MS, Δ*tom70*+pYX142-*Hs*Tom70+pYX123-Orf9b (or pYX123 empty vector/pYX142 empty vector) cells were cultured in SLac medium. Cells were diluted continuously to keep them in the exponential growth phase. Orf9b expression was induced with galactose (final concentration 0.5%). After 16 h of induction, 10 OD_{600} of each culture were harvested (5,000 g, 5 min, RT), washed with sterile water, and shock-frozen with liquid nitrogen. Samples were stored at −80°C for further analysis. MS samples were prepared according to a published protocol with minor adaptations (Kulak et al., 2014). To analyze the proteome changes upon Orf9b expression, cell lysates were prepared in 100 µl lysis buffer (6 M guanidinium chloride, 10 mM TCEP-HCl, 40 mM chloroacetamide, and 100 mM Tris, pH 8.5) using a FastPrep-24 5 G homogenizer (MP Biomedicals) with three cycles of 20 s, speed 8.0 m/s, 120 s breaks, and glass beads (Ø 0.5 mm) at 4°C. Samples were heated for 10 min at 96°C and afterward centrifuged twice for 5 min at 16,000 *g*. In between, the supernatant was transferred to fresh Eppendorf tubes to remove all remaining glass beads. Protein concentrations were measured using the Pierce BCA Protein Assay (#23225; Thermo Fisher Scientific). For protein digestion, 25 µg of protein was diluted 1:10 with LT-digestion buffer (10% acetonitrile, 25 mM Tris, pH 8.8). Trypsin (#T6567; Sigma-Aldrich) and Lys-C (#125-05061; Wako) were added to the samples (1:50 wt/wt). Samples were incubated overnight at 37°C and 700 rpm. After 16 h, fresh Trypsin (1:100 wt/wt) was added for 30 min (37°C, 700 rpm). pH of samples was adjusted to pH < 2 with trifluoroacetic acid (10%) and samples were centrifuged for 3 min at 16,000 *g* and RT. Desalting/mixed-Phase cleanup was performed with three layers of styrenedivinylbenzene reverse phase sulfonate stage tips (cat 2241). Samples were dried down in speed-vac and resolubilized in 12 µl buffer A++ (buffer A [0.1% formic acid] and buffer A* [2% acetonitrile and 0.1% trifluoracetic acid] in a ratio of 9:1). 4 µl of the resolubilize peptides was separated on a 50-cm long reverse phase column with an inner diameter of 75 µm packed in-house with C18 material (Dr. Maisch GmbH). Chromatography was performed with an Easy-nLC 1200 System directly coupled to a Q Exactive HF mass spectrometer via a Nanoflex source (Sonation). A nonlinear 180-min gradient of 2–95% buffer b (80% (vol/vol) acetonitrile, 0.1% (vol/vol) formic acid) was applied using a constant flow rate of 250 nl/min. All MS data were recorded with a data-dependent acquisition strategy (see raw files available at ProteomExchange for details).

MS data processing

MS data obtained from yeast samples were processed using the MaxQuant software (version 2.0.1.0; Cox and Mann, 2008; Cox et al., 2011; Tyanova et al., 2016). Peak lists were searched against the yeast Uniprot FASTA database and the amino acid sequence of human Tom70 and Orf9b.

Statistical analysis of MS data

Protein groups identified in human and yeast samples were processed and analyzed in parallel using the R programming language (version 4.2.1, R Core Team, 2018). First, protein groups were filtered to remove contaminants, reverse hits, and proteins identified by site only as well as proteins that were identified in less than three replicates ($N = 4$) of every condition. This resulted in 4,316 (human galactose), 3,697 (human glucose), and 3,910 (yeast) robustly identified protein groups in human

samples grown in galactose or glucose and yeast samples, respectively. Next, the protein group's label-free quantification (LFQ) intensities were log_2-transformed and normalized between samples using fast linear loess normalization (Ballman et al., 2004) as implemented in the *limma* R-package (Ritchie et al., 2015). Finally, missing values were imputed by the minimum values observed as implemented in the *imputeLCMD* package (Lazar, 2015) function *impute.MinDet* using 1% percentile of each replicate respectively to estimate the minima. Only those missing values with no corresponding valid values in a quadruplicate of a condition were imputed. Since in this imputation scheme it is assumed that missing values are left-censored, this distinction was made to avoid placing minima where values are potentially more likely to be missing at random. In total, 251–362 values were imputed this way in human samples grown in galactose, 141–207 in those grown in glucose, and 110–147 in the yeast data set.

Protein groups were statistically analyzed using pairwise, two-sided Welch's *t* tests on the processed LFQ intensities between the replicates of respective control and treatment conditions. Only comparisons with non-imputed values in either the control or treatment condition were tested. The resulting P values were adjusted for multiple testing using the Benjamini-Hochberg procedure (Benjamini and Hochberg, 1995) and are listed together with all test results in Table S1.

Principal component analysis was carried out for each data set using the package *pcaMethods* (Stacklies et al., 2007) on the processed and standardized LFQ intensities of those protein groups with an ANOVA F-statistic P value <0.05 between all replicate groups to filter for proteins with a discernable degree of variance between conditions.

Western blot analyses were independently replicated with similar results, and representative data are shown in the figures. Quantification was performed with Bio-Rad Image lab software, and significance testing was performed with Student's *t* test.

Analyses of import experiments into semi-intact cells were independently replicated with similar results, and representative data are shown in the figures. Quantification was performed with the ImageQuant Software or ImageJ/Fiji, and significance testing was performed with Student's *t* test.

Sample preparation and mass spectrometric identification of proteins in human cells

For whole-cell MS of human cells, HEK Flp-In T-REx-293 WT or *Tom70* KD cells were cultured in DMEM supplemented with glucose or galactose for at least 2 wk. Expression of Orf9b-HA was induced with 1 µg/ml doxycycline for 4 d before lysis. Cells were seeded onto 6-well plates and lysed after reaching confluence. Cells were washed once with PBS, scratched off, and transferred into a 1.5-ml reaction tube. After centrifugation for 7 min at 300 *g*, cell pellets were resuspended in lysis buffer (4% SDS in PBS, supplemented with protease inhibitor), sonicated, and boiled for 5 min at 96°C. To remove detergents, proteins were precipitated with acetone at −80°C overnight, washed twice, and air-dried before in-solution digest. For this, pellets were resuspended in urea lysis buffer (8 M urea, 50 mM triethylammoniumbicarbonate buffer supplemented with protease inhibitor) and sonicated. Protein concentrations were determined using Pierce 660 nm Protein Assay Reagent (#22660; Thermo Fisher Scientific). 50 µg of the sample was reduced by DTT for 1 h at 37°C and afterward modified by chloroacetamide for 30 min at RT. Proteins were first digested with Lys-C at an enzyme:substrate ratio of 1:75 for 4 h at 25°C before dilution with triethylammoniumbicarbonate buffer to a urea concentration <2 M. Finally, samples were digested by addition of trypsin at an enzyme/substrate ratio of 1:75 at 25°C overnight. Digestion was terminated by the addition of 1% formic acid. Desalting/mixed-phase cleanup was performed with two-layer styrenedivinylbenzene reverse phase sulfonate stage tips.

All samples were analyzed by the CECAD proteomics facility on a Q Exactive Plus Orbitrap mass spectrometer that was coupled to an EASY nLC (both Thermo Fisher Scientific). Peptides were loaded with solvent A (0.1% formic acid in water) onto an in-house packed analytical column (50 cm, 75 µm inner diameter, filled with 2.7 µm Poroshell EC120 C18; Agilent). Peptides were chromatographically separated at a constant flow rate of 250 nl/min using the following gradient: 3–5% solvent B (0.1% formic acid in 80% acetonitrile) within 1.0 min, 5–30% solvent B within 121.0 min, 30–40% solvent B within 19.0 min, 40–95% solvent B within 1.0 min, followed by washing and column equilibration. The mass spectrometer was operated in data-dependent acquisition mode. The MS1 survey scan was acquired from 300 to 1,750 m/z at a resolution of 70,000. The top 10 most abundant peptides were isolated within a 1.8-Th window and subjected to higher-energy C-trap dissociation fragmentation at a normalized collision energy of 27%. The automatic gain control target was set to 5e5 charges, allowing a maximum injection time of 55 ms. Product ions were detected in the Orbitrap at a resolution of 17,500. Precursors were dynamically excluded for 25.0 s.

All mass spectrometric raw data were processed with Maxquant (version 2.0.3.0; Tyanova et al., 2016) using default parameters against the Uniprot canonical Human database (UP5640, downloaded January 20, 2022) with the match-between-runs option enabled between replicates. A follow-up analysis was done in Perseus 1.6.15 (Tyanova et al., 2016). Hits from the decoy database, the contaminant list, and those only identified by modified peptides were removed. Afterward, results were filtered for data completeness in replicate groups, and LFQ values were imputed using Sigma-Aldrich downshift with standard settings. Finally, false discovery rate–controlled *T* tests between sample groups were performed with s0 = 0.2. For the annotation of mitochondrial proteins, the MitoCarta3.0 database (Rath et al., 2021) was used.

Fluorescence microscopy and image analysis (yeast)

Yeast strains were cultured in synthetic media to mid-log phase. Orf9b expression was induced by the addition of 0.5% galactose to the cultures. Cells were harvested after 4 h of galactose induction and images were taken using the Leica-Thunder imager 3D live cell using 100× oil objective (Leica Microsystems 0.55 S28 LEICA; Inverse, DMi 8 HC; PL Apo 100×/1.44 Oil CDRR CS, LAS X). Colocalization analysis of the Su9-mNeonGreen (green) signal and Orf9b-mScarlet (red) signal was performed using the ImageJ/Fiji Coloc2 plugin (Schindelin et al., 2012). Regions of interest (ROIs) outlining the cells were selected, followed by

measurement of Pearson's correlation coefficient in the selected ROIs. For the mitochondrial area analysis, an ImageJ/Fiji macro based on thresholding was created. ROIs defining the cells were selected manually for each image and the area was calculated using the analyze particles function in ImageJ/Fiji. Correlation and area results were plotted in RStudio using the Beeswarm package. Statistical analysis was performed in RStudio using the Kruskal–Wallis rank sum test followed by Dunn's test adjusted with the Benjamini–Hochberg method.

Fluorescence microscopy and image analysis (human cells)

HEK293 Flp-In T-REx cells expressing HA-tagged Orf9b were cultured on poly-l-lysine–coated coverslips for 24 h. Protein expression was induced by the addition of 1 µg/ml doxycycline after 8 h of culture. To inhibit the proteasome, cells were treated with 5 µM MG132 (Sigma-Aldrich) or with DMSO as control for 2 h at 37°C before staining. Before fixation, the cells were incubated with MitoTracker Red (Thermo Fisher Scientific) for 1 h at 37°C. Fixation was performed with 4% paraformaldehyde for 15 min. Then, cell membranes were permeabilized with blocking buffer (10 mM Hepes, pH 7.4, 3% BSA, 0.3% Triton X-100) for 1 h. Cells were washed and incubated with primary (anti-HA, SAB4300603; Sigma-Aldrich) and secondary antibodies (anti-rabbit, AlexaFluor 488) for 1 h at room temperature. Then, the cells were washed and stained with DAPI for 15 min at room temperature followed by conserving the samples with mounting medium (25% glycerol, 10% polyvinyl alcohol, 100 mM TRIS, and 2.5% 1,4-diazabicyclo-2,2,2-octan). Cells were analyzed by confocal fluorescence microscopy (Leica Microsystems TCS SP8; Inverse, DMi 8 CS; PL Apo 63×/1.40 Oil CS2, LAS X) at room temperature using oil as the imaging medium. Images were acquired and processed using the software LAS X and OMERO.insight, respectively. Colocalization of the HA-signal and MitoTracker was quantified using FiJi (Schindelin et al., 2012) and the Just Another Co-localization Plugin (Bolte and Cordelières, 2006), and represented as the Manders' overlap coefficient (M1) for single cells.

Reviewer account details

Project Name: HEK293 WT and TOM70 KD cell lines expressing HA-tagged Orf9b grown on glucose media (Project accession: PXD040491)

Project Name: HEK293 WT and TOM70 KD cell lines expressing HA-tagged Orf9b grown on galactose media (Project accession: PXD040494)

Project Name: The Orf9b protein of SARS-CoV-2 modulates mitochondrial protein biogenesis—Yeast Data Set (Project accession: PXD039850)

Online supplemental material

Fig. S1 shows that Tom70 can be efficiently depleted in HEK293 cells. Fig. S2 shows the proteome of glucose-grown cells is only moderately affected by Tom70 depletion. Fig. S3 shows the alignment of the sequences of Tom70 human and yeast homologs. Fig. S4 shows that the ATP/ADP carrier protein (Pet9) is not efficiently imported into the mitochondria of the semi-intact cell. Table S1 shows proteomic data from MS. Table S2 shows the strains and plasmids.

Data availability

The MS proteomics data (see also Table S1) have been deposited to the ProteomeXchange Consortium via the PRIDE (Perez-Riverol et al., 2019) partner repository with the dataset identifier PXD040491 (Orf9b expression in human cells, glucose), PXD040494 (Orf9b expression in human cells, galactose), and PXD039850 (Orf9b expression in yeast cells).

Acknowledgments

We thank Lena Krämer and Christian Koch for help with the *PUP2* depletion. We thank Anja Wittmann for technical support throughout the project, and the CECAD Proteome and Imaging Facilities for the provision of instrumentation, training, and technical support. We thank the Center of MS Analytics in Kaiserslautern for the proteome analysis of the yeast samples.

This study was financially supported by the European Research Council (ERC 101052639 MitoCyto to J.M. Herrmann), the Deutsche Forschungsgemeinschaft (GRK2737-STRESSistance to J.M. Herrmann and Z. Storchova), the Deutsche Forschungsgemeinschaft (RI2150/5-1 project number 435235019, RI2150/2-2 project number 251546152, RTG2550/1-RELOC project number 411422114, and CRC1218 project number 269925409 to J. Riemer), and the Landesforschungsinitiative Rheinland-Pfalz BioComp (to J.M. Herrmann, M. Räschle, and Z. Storchova). This work was supported by the large instrument grant INST 216/1163-1 FUGG by the German Research Foundation to the CECAD proteomics facility.

Author contributions: S. Lenhard, S. Gerlich, E. Peker, and J. Faust designed, cloned, and verified the constructs and strains; J. Riemer and J.M. Herrmann conceived the project; S. Gerlich, C. Zarges, M. Räschle, and Z. Storchova carried out the MS-based proteomics; S. Lenhard, S. Gerlich, and J.-E. Bökenkamp performed the bioinformatical analysis of the MS data; S. Gerlich, E. Peker, and C. Zarges carried out the biochemical experiments in the HEK293 cell model; S. Lenhard, S. Rödl, and J.L. carried out the biochemical experiments in yeast; S. Gerlich and A. Khan carried out the fluorescence microscopy experiments and the image analysis; S. Lenhard, S. Gerlich, J. Riemer, and J.M. Herrmann analyzed the data; S. Lenhard, J. Riemer, and J.M. Herrmann wrote the manuscript with the help and input of all authors.

Disclosures: The authors declare no competing interests exist.

Submitted: 1 March 2023
Revised: 6 July 2023
Accepted: 7 August 2023

References

Backes, S., S. Hess, F. Boos, M.W. Woellhaf, S. Gödel, M. Jung, T. Mühlhaus, and J.M. Herrmann. 2018. Tom70 enhances mitochondrial preprotein import efficiency by binding to internal targeting sequences. *J. Cell Biol.* 217:1369–1382. https://doi.org/10.1083/jcb.201708044

Backes, S., Y.S. Bykov, T. Flohr, M. Räschle, J. Zhou, S. Lenhard, L. Krämer, T. Mühlhaus, C. Bibi, C. Jann, et al. 2021. The chaperone-binding activity of the mitochondrial surface receptor Tom70 protects the cytosol

against mitoprotein-induced stress. *Cell Rep.* 35:108936. https://doi.org/10.1016/j.celrep.2021.108936

Ballman, K.V., D.E. Grill, A.L. Oberg, and T.M. Therneau. 2004. Faster cyclic loess: Normalizing RNA arrays via linear models. *Bioinformatics*. 20: 2778–2786. https://doi.org/10.1093/bioinformatics/bth327

Benjamini, Y., and Y. Hochberg. 1995. Controlling the false discovery rate: A practical and powerful approach to multiple testing. *J. R. Stat. Soc. B*. 57: 289–300. https://doi.org/10.1111/j.2517-6161.1995.tb02031.x

Bhowal, C., S. Ghosh, D. Ghatak, and R. De. 2022. Pathophysiological involvement of host mitochondria in SARS-CoV-2 infection that causes COVID-19: A comprehensive evidential insight. *Mol. Cell. Biochem.*. 478: 1325–1343. https://doi.org/10.1007/s11010-022-04593-z

Bojkova, D., K. Klann, B. Koch, M. Widera, D. Krause, S. Ciesek, J. Cinatl, and C. Münch. 2020. Proteomics of SARS-CoV-2-infected host cells reveals therapy targets. *Nature*. 583:469–472. https://doi.org/10.1038/s41586-020-2332-7

Bolte, S., and F.P. Cordelières. 2006. A guided tour into subcellular colocalization analysis in light microscopy. *J. Microsc.* 224:213–232. https://doi.org/10.1111/j.1365-2818.2006.01706.x

Boos, F., T. Mühlhaus, and J.M. Herrmann. 2018. Detection of internal matrix targeting signal-like sequences (iMTS-Ls) in mitochondrial precursor proteins using the TargetP prediction tool. *Bio Protoc.* 8:e2474. https://doi.org/10.21769/BioProtoc.2474

Botman, D., D.H. de Groot, P. Schmidt, J. Goedhart, and B. Teusink. 2019. In vivo characterisation of fluorescent proteins in budding yeast. *Sci. Rep.* 9:2234. https://doi.org/10.1038/s41598-019-38913-z

Böttinger, L., A. Gornicka, T. Czerwik, P. Bragoszewski, A. Loniewska-Lwowska, A. Schulze-Specking, K.N. Truscott, B. Guiard, D. Milenkovic, and A. Chacinska. 2012. In vivo evidence for cooperation of Mia40 and Erv1 in the oxidation of mitochondrial proteins. *Mol. Biol. Cell*. 23: 3957–3969. https://doi.org/10.1091/mbc.e12-05-0358

Brandherm, L., A.M. Kobaš, M. Klöhn, Y. Brüggemann, S. Pfaender, J. Rassow, and S. Kreimendahl. 2021. Phosphorylation of SARS-CoV-2 Orf9b regulates its targeting to two binding sites in TOM70 and recruitment of Hsp90. *Int. J. Mol. Sci.* 22:9233. https://doi.org/10.3390/ijms22179233

Burtscher, J., M. Burtscher, and G.P. Millet. 2021. The central role of mitochondrial fitness on antiviral defenses: An advocacy for physical activity during the COVID-19 pandemic. *Redox Biol.* 43:101976. https://doi.org/10.1016/j.redox.2021.101976

Chan, N.C., V.A. Likić, R.F. Waller, T.D. Mulhern, and T. Lithgow. 2006. The C-terminal TPR domain of Tom70 defines a family of mitochondrial protein import receptors found only in animals and fungi. *J. Mol. Biol.* 358:1010–1022. https://doi.org/10.1016/j.jmb.2006.02.062

Chang, X., N.I. Ismail, A. Rahman, D. Xu, R.W.Y. Chan, S.G. Ong, and S.B. Ong. 2022. Long COVID-19 and the heart: Is cardiac mitochondria the missing link? *Antioxid. Redox Signal.* 38:599–618. https://doi.org/10.1089/ars.2022.0126

Cox, J., and M. Mann. 2008. MaxQuant enables high peptide identification rates, individualized p.p.b.-range mass accuracies and proteome-wide protein quantification. *Nat. Biotechnol.* 26:1367–1372. https://doi.org/10.1038/nbt.1511

Cox, J., N. Neuhauser, A. Michalski, R.A. Scheltema, J.V. Olsen, and M. Mann. 2011. Andromeda: A peptide search engine integrated into the MaxQuant environment. *J. Proteome Res.* 10:1794–1805. https://doi.org/10.1021/pr101065j

Denaro, C.A., Y.I. Haloush, S.Y. Hsiao, J.J. Orgera, T. Osorio, L.M. Riggs, J.W. Sassaman, S.A. Williams, A.R. Monte Carlo III, R.T. Da Costa, et al. 2022. COVID-19 and neurodegeneration: The mitochondrial connection. *Aging Cell*. 21:e13727. https://doi.org/10.1111/acel.13727

Edgar, R.C. 2004. Muscle: Multiple sequence alignment with high accuracy and high throughput. *Nucleic Acids Res.* 32:1792–1797. https://doi.org/10.1093/nar/gkh340

Eisenberg-Bord, M., N. Zung, J. Collado, L. Drwesh, E.J. Fenech, A. Fadel, N. Dezorella, Y.S. Bykov, D. Rapaport, R. Fernandez-Busnadiego, and M. Schuldiner. 2021. Cnm1 mediates nucleus-mitochondria contact site formation in response to phospholipid levels. *J. Cell Biol.* 220:e202104100. https://doi.org/10.1083/jcb.202104100

Elbaz-Alon, Y., M. Eisenberg-Bord, V. Shinder, S.B. Stiller, E. Shimoni, N. Wiedemann, T. Geiger, and M. Schuldiner. 2015. Lam6 regulates the extent of contacts between organelles. *Cell Rep.* 12:7–14. https://doi.org/10.1016/j.celrep.2015.06.022

Filadi, R., N.S. Leal, B. Schreiner, A. Rossi, G. Dentoni, C.M. Pinho, B. Wiehager, D. Cieri, T. Calì, P. Pizzo, and M. Ankarcrona. 2018. TOM70 sustains cell bioenergetics by promoting IP3R3-mediated ER to mitochondria Ca^{2+} transfer. *Curr. Biol.* 28:369–382.e6. https://doi.org/10.1016/j.cub.2017.12.047

Finkel, Y., O. Mizrahi, A. Nachshon, S. Weingarten-Gabbay, D. Morgenstern, Y. Yahalom-Ronen, H. Tamir, H. Achdout, D. Stein, O. Israeli, et al. 2021. The coding capacity of SARS-CoV-2. *Nature*. 589:125–130. https://doi.org/10.1038/s41586-020-2739-1

Gao, X., K. Zhu, B. Qin, V. Olieric, M. Wang, and S. Cui. 2021. Crystal structure of SARS-CoV-2 Orf9b in complex with human TOM70 suggests unusual virus-host interactions. *Nat. Commun.* 12:2843. https://doi.org/10.1038/s41467-021-23118-8

Gibellini, L., S. De Biasi, A. Paolini, R. Borella, F. Boraldi, M. Mattioli, D. Lo Tartaro, L. Fidanza, A. Caro-Maldonado, M. Meschiari, et al. 2020. Altered bioenergetics and mitochondrial dysfunction of monocytes in patients with COVID-19 pneumonia. *EMBO Mol. Med.* 12:e13001. https://doi.org/10.15252/emmm.202013001

Gietz, D., A. St Jean, R.A. Woods, and R.H. Schiestl. 1992. Improved method for high efficiency transformation of intact yeast cells. *Nucleic Acids Res.* 20:1425. https://doi.org/10.1093/nar/20.6.1425

Goldmacher, V.S., L.M. Bartle, A. Skaletskaya, C.A. Dionne, N.L. Kedersha, C.A. Vater, J.W. Han, R.J. Lutz, S. Watanabe, E.D. Cahir McFarland, et al. 1999. A cytomegalovirus-encoded mitochondria-localized inhibitor of apoptosis structurally unrelated to Bcl-2. *Proc. Natl. Acad. Sci. USA*. 96: 12536–12541. https://doi.org/10.1073/pnas.96.22.12536

Guna, A., T.A. Stevens, A.J. Inglis, J.M. Replogle, T.K. Esantsi, G. Muthukumar, K.C.L. Shaffer, M.L. Wang, A.N. Pogson, J.J. Jones, et al. 2022. MTCH2 is a mitochondrial outer membrane protein insertase. *Science*. 378:317–322. https://doi.org/10.1126/science.add1856

Hansen, K.G., N. Aviram, J. Laborenz, C. Bibi, M. Meyer, A. Spang, M. Schuldiner, and J.M. Herrmann. 2018. An ER surface retrieval pathway safeguards the import of mitochondrial membrane proteins in yeast. *Science*. 361:1118–1122. https://doi.org/10.1126/science.aar8174

Hase, T., H. Riezman, K. Suda, and G. Schatz. 1983. Import of proteins into mitochondria: Nucleotide sequence of the gene for a 70-kd protein of the yeast mitochondrial outer membrane. *EMBO J.* 2:2169–2172. https://doi.org/10.1002/j.1460-2075.1983.tb01718.x

Hines, V., and G. Schatz. 1993. Precursor binding to yeast mitochondria. A general role for the outer membrane protein Mas70p. *J. Biol. Chem.* 268: 449–454. https://doi.org/10.1016/S0021-9258(18)54172-7

Hossain, A., S. Akter, A.A. Rashid, S. Khair, and A.S.M.R.U. Alam. 2022. Unique mutations in SARS-CoV-2 Omicron subvariants' non-spike proteins: Potential impacts on viral pathogenesis and host immune evasion. *Microb. Pathog.* 170:105699. https://doi.org/10.1016/j.micpath.2022.105699

Huang, Y.J., Y.H. Jan, Y.C. Chang, H.F. Tsai, A.T. Wu, C.L. Chen, and M. Hsiao. 2019. ATP synthase subunit epsilon overexpression promotes metastasis by modulating AMPK signaling to induce epithelial-to-mesenchymal transition and is a poor prognostic marker in colorectal cancer patients. *J. Clin. Med.* 8:1070. https://doi.org/10.3390/jcm8071070

Hurtado-López, L.M., F. Fernández-Ramírez, E. Martínez-Peñafiel, J.D. Carrillo Ruiz, and N.E. Herrera González. 2015. Molecular analysis by gene expression of mitochondrial ATPase subunits in papillary thyroid cancer: Is ATP5E transcript a possible early tumor marker? *Med. Sci. Monit.* 21:1745–1751. https://doi.org/10.12659/MSM.893597

Jacobs, J.L., and C.B. Coyne. 2013. Mechanisms of MAVS regulation at the mitochondrial membrane. *J. Mol. Biol.* 425:5009–5019. https://doi.org/10.1016/j.jmb.2013.10.007

Jiang, H.W., H.N. Zhang, Q.F. Meng, J. Xie, Y. Li, H. Chen, Y.X. Zheng, X.N. Wang, H. Qi, J. Zhang, et al. 2020. SARS-CoV-2 Orf9b suppresses type I interferon responses by targeting TOM70. *Cell. Mol. Immunol.* 17: 998–1000. https://doi.org/10.1038/s41423-020-0514-8

Kasahara, A., and L. Scorrano. 2014. Mitochondria: From cell death executioners to regulators of cell differentiation. *Trends Cell Biol.* 24:761–770. https://doi.org/10.1016/j.tcb.2014.08.005

Kee, J., S. Thudium, D.M. Renner, K. Glastad, K. Palozola, Z. Zhang, Y. Li, Y. Lan, J. Cesare, A. Poleshko, et al. 2022. SARS-CoV-2 disrupts host epigenetic regulation via histone mimicry. *Nature*. 610:381–388. https://doi.org/10.1038/s41586-022-05282-z

Komiya, T., S. Rospert, G. Schatz, and K. Mihara. 1997. Binding of mitochondrial precursor proteins to the cytoplasmic domains of the import receptors Tom70 and Tom20 is determined by cytoplasmic chaperones. *EMBO J.* 16:4267–4275. https://doi.org/10.1093/emboj/16.14.4267

Kondo-Okamoto, N., J.M. Shaw, and K. Okamoto. 2008. Tetratricopeptide repeat proteins Tom70 and Tom71 mediate yeast mitochondrial morphogenesis. *EMBO Rep.* 9:63–69. https://doi.org/10.1038/sj.embor.7401113

Kreimendahl, S., and J. Rassow. 2020. The mitochondrial outer membrane protein tom70-mediator in protein traffic, membrane contact sites and

innate immunity. *Int. J. Mol. Sci.* 21:7262. https://doi.org/10.3390/ijms21197262

Kulak, N.A., G. Pichler, I. Paron, N. Nagaraj, and M. Mann. 2014. Minimal, encapsulated proteomic-sample processing applied to copy-number estimation in eukaryotic cells. *Nat. Methods.* 11:319–324. https://doi.org/10.1038/nmeth.2834

Laborenz, J., K. Hansen, C. Prescianotto-Baschong, A. Spang, and J.M. Herrmann. 2019. In vitro import experiments with semi-intact cells suggest a role of the Sec61 paralog Ssh1 in mitochondrial biogenesis. *Biol. Chem.* 400:1229–1240. https://doi.org/10.1515/hsz-2019-0196

Lazar, C. 2015. ImputeLCMD: A Collection of Methods for Left-Censored Missing Data Imputation. R Package, Version 2.0. http://CRAN.R-project.org/package=imputeLCMD.

Li, J., X. Qian, J. Hu, and B. Sha. 2009. Molecular chaperone Hsp70/Hsp90 prepares the mitochondrial outer membrane translocon receptor Tom71 for preprotein loading. *J. Biol. Chem.* 284:23852–23859. https://doi.org/10.1074/jbc.M109.023986

Li, J., W. Cui, and B. Sha. 2010. The structural plasticity of Tom71 for mitochondrial precursor translocations. *Acta Crystallogr. Sect. F Struct. Biol. Cryst. Commun.* 66:985–989. https://doi.org/10.1107/S1744309110025522

Li, X., J. Straub, T.C. Medeiros, C. Mehra, F. den Brave, E. Peker, I. Atanassov, K. Stillger, J.B. Michaelis, E. Burbridge, et al. 2022. Mitochondria shed their outer membrane in response to infection-induced stress. *Science.* 375:eabi4343. https://doi.org/10.1126/science.abi4343

Liu, X.Y., B. Wei, H.X. Shi, Y.F. Shan, and C. Wang. 2010. Tom70 mediates activation of interferon regulatory factor 3 on mitochondria. *Cell Res.* 20:994–1011. https://doi.org/10.1038/cr.2010.103

Liu, Q., C.E. Chang, A.C. Wooldredge, B. Fong, B.K. Kennedy, and C. Zhou. 2022. Tom70-based transcriptional regulation of mitochondrial biogenesis and aging. *Elife.* 11:e75658. https://doi.org/10.7554/eLife.75658

Mårtensson, C.U., C. Priesnitz, J. Song, L. Ellenrieder, K.N. Doan, F. Boos, A. Floerchinger, N. Zufall, S. Oeljeklaus, B. Warscheid, and T. Becker. 2019. Mitochondrial protein translocation-associated degradation. *Nature.* 569:679–683. https://doi.org/10.1038/s41586-019-1227-y

McWhirter, S.M., B.R. Tenoever, and T. Maniatis. 2005. Connecting mitochondria and innate immunity. *Cell.* 122:645–647. https://doi.org/10.1016/j.cell.2005.08.026

Miserey-Lenkei, S., K. Trajkovic, J.M. D'Ambrosio, A.J. Patel, A. Čopič, P. Mathur, K. Schauer, B. Goud, V. Albanèse, R. Gautier, et al. 2021. A comprehensive library of fluorescent constructs of SARS-CoV-2 proteins and their initial characterisation in different cell types. *Biol. Cell.* 113:311–328. https://doi.org/10.1111/boc.202000158

Moehlman, A.T., and R.J. Youle. 2020. Mitochondrial quality control and restraining innate immunity. *Annu. Rev. Cell Dev. Biol.* 36:265–289. https://doi.org/10.1146/annurev-cellbio-021820-101354

Morgenstern, M., S.B. Stiller, P. Lübbert, C.D. Peikert, S. Dannenmaier, F. Drepper, U. Weill, P. Höß, R. Feuerstein, M. Gebert, et al. 2017. Definition of a high-confidence mitochondrial proteome at quantitative scale. *Cell Rep.* 19:2836–2852. https://doi.org/10.1016/j.celrep.2017.06.014

Morgenstern, M., C.D. Peikert, P. Lübbert, I. Suppanz, C. Klemm, O. Alka, C. Steiert, N. Naumenko, A. Schendzielorz, L. Melchionda, et al. 2021. Quantitative high-confidence human mitochondrial proteome and its dynamics in cellular context. *Cell Metabol.* 33:2464–2483.e18. https://doi.org/10.1016/j.cmet.2021.11.001

Murley, A., R.D. Sarsam, A. Toulmay, J. Yamada, W.A. Prinz, and J. Nunnari. 2015. Ltc1 is an ER-localized sterol transporter and a component of ER-mitochondria and ER-vacuole contacts. *J. Cell Biol.* 209:539–548. https://doi.org/10.1083/jcb.201502033

Murley, A., J. Yamada, B.J. Niles, A. Toulmay, W.A. Prinz, T. Powers, and J. Nunnari. 2017. Sterol transporters at membrane contact sites regulate TORC1 and TORC2 signaling. *J. Cell Biol.* 216:2679–2689. https://doi.org/10.1083/jcb.201610032

Murschall, L.M., E. Peker, T. MacVicar, T. Langer, and J. Riemer. 2021. Protein import assay into mitochondria isolated from human cells. *Bio Protoc.* 11:e4057. https://doi.org/10.21769/BioProtoc.4057

Neufeldt, C.J., B. Cerikan, M. Cortese, J. Frankish, J.Y. Lee, A. Plociennikowska, F. Heigwer, V. Prasad, S. Joecks, S.S. Burkart, et al. 2022. SARS-CoV-2 infection induces a pro-inflammatory cytokine response through cGAS-STING and NF-κB. *Commun. Biol.* 5:45. https://doi.org/10.1038/s42003-021-02983-5

Opaliński, Ł., J. Song, C. Priesnitz, L.S. Wenz, S. Oeljeklaus, B. Warscheid, N. Pfanner, and T. Becker. 2018. Recruitment of cytosolic J-proteins by TOM receptors promotes mitochondrial protein biogenesis. *Cell Rep.* 25:2036–2043.e5. https://doi.org/10.1016/j.celrep.2018.10.083

Perez-Riverol, Y., A. Csordas, J. Bai, M. Bernal-Llinares, S. Hewapathirana, D.J. Kundu, A. Inuganti, J. Griss, G. Mayer, M. Eisenacher, et al. 2019. The PRIDE database and related tools and resources in 2019: Improving support for quantification data. *Nucleic Acids Res.* 47:D442–D450. https://doi.org/10.1093/nar/gky1106

Ramage, L., T. Junne, K. Hahne, T. Lithgow, and G. Schatz. 1993. Functional cooperation of mitochondrial protein import receptors in yeast. *EMBO J.* 12:4115–4123. https://doi.org/10.1002/j.1460-2075.1993.tb06095.x

Ran, F.A., P.D. Hsu, J. Wright, V. Agarwala, D.A. Scott, and F. Zhang. 2013. Genome engineering using the CRISPR-Cas9 system. *Nat. Protoc.* 8:2281–2308. https://doi.org/10.1038/nprot.2013.143

Rath, S., R. Sharma, R. Gupta, T. Ast, C. Chan, T.J. Durham, R.P. Goodman, Z. Grabarek, M.E. Haas, W.H.W. Hung, et al. 2021. MitoCarta3.0: An updated mitochondrial proteome now with sub-organelle localization and pathway annotations. *Nucleic Acids Res.* 49:D1541–D1547. https://doi.org/10.1093/nar/gkaa1011

Ritchie, M.E., B. Phipson, D. Wu, Y. Hu, C.W. Law, W. Shi, and G.K. Smyth. 2015. Limma powers differential expression analyses for RNA-sequencing and microarray studies. *Nucleic Acids Res.* 43:e47. https://doi.org/10.1093/nar/gkv007

R Core Team. 2018. R: A language and environment for statistical computing. R Foundation for Statistical Computing, Vienna, Austria. https://www.R-project.org/.

Schindelin, J., I. Arganda-Carreras, E. Frise, V. Kaynig, M. Longair, T. Pietzsch, S. Preibisch, C. Rueden, S. Saalfeld, B. Schmid, et al. 2012. Fiji: An open-source platform for biological-image analysis. *Nat. Methods.* 9:676–682. https://doi.org/10.1038/nmeth.2019

Schlenstedt, G., E. Hurt, V. Doye, and P.A. Silver. 1993. Reconstitution of nuclear protein transport with semi-intact yeast cells. *J. Cell Biol.* 123:785–798. https://doi.org/10.1083/jcb.123.4.785

Schlossmann, J., K. Dietmeier, N. Pfanner, and W. Neupert. 1994. Specific recognition of mitochondrial preproteins by the cytosolic domain of the import receptor MOM72. *J. Biol. Chem.* 269:11893–11901. https://doi.org/10.1016/S0021-9258(17)32657-1

Schneider, K., D. Zimmer, H. Nielsen, J.M. Herrmann, and T. Mühlhaus. 2021. iMLP, a predictor for internal matrix targeting-like sequences in mitochondrial proteins. *Biol. Chem.* 402:937–943. https://doi.org/10.1515/hsz-2021-0185

Sender, R., Y.M. Bar-On, S. Gleizer, B. Bernshtein, A. Flamholz, R. Phillips, and R. Milo. 2021. The total number and mass of SARS-CoV-2 virions. *Proc. Natl. Acad. Sci. USA.* 118:e2024815118. https://doi.org/10.1073/pnas.2024815118

Shi, C.S., H.Y. Qi, C. Boularan, N.N. Huang, M. Abu-Asab, J.H. Shelhamer, and J.H. Kehrl. 2014. SARS-coronavirus open reading frame-9b suppresses innate immunity by targeting mitochondria and the MAVS/TRAF3/TRAF6 signalosome. *J. Immunol.* 193:3080–3089. https://doi.org/10.4049/jimmunol.1303196

Shi, Y., B. Yuan, N. Qi, W. Zhu, J. Su, X. Li, P. Qi, D. Zhang, and F. Hou. 2015. An autoinhibitory mechanism modulates MAVS activity in antiviral innate immune response. *Nat. Commun.* 6:7811. https://doi.org/10.1038/ncomms8811

Sikorski, R.S., and P. Hieter. 1989. A system of shuttle vectors and yeast host strains designed for efficient manipulation of DNA in Saccharomyces cerevisiae. *Genetics.* 122:19–27. https://doi.org/10.1093/genetics/122.1.19

Smith, J.D., S. Suresh, U. Schlecht, M. Wu, O. Wagih, G. Peltz, R.W. Davis, L.M. Steinmetz, L. Parts, and R.P. St Onge. 2016. Quantitative CRISPR interference screens in yeast identify chemical-genetic interactions and new rules for guide RNA design. *Genome Biol.* 17:45. https://doi.org/10.1186/s13059-016-0900-9

Stacklies, W., H. Redestig, M. Scholz, D. Walther, and J. Selbig. 2007. pcaMethods--a bioconductor package providing PCA methods for incomplete data. *Bioinformatics.* 23:1164–1167. https://doi.org/10.1093/bioinformatics/btm069

Steger, H.F., T. Söllner, M. Kiebler, K.A. Dietmeier, R. Pfaller, K.S. Trülzsch, M. Tropschug, W. Neupert, and N. Pfanner. 1990. Import of ADP/ATP carrier into mitochondria: Two receptors act in parallel. *J. Cell Biol.* 111:2353–2363. https://doi.org/10.1083/jcb.111.6.2353

Stukalov, A., V. Girault, V. Grass, O. Karayel, V. Bergant, C. Urban, D.A. Haas, Y. Huang, L. Oubraham, A. Wang, et al. 2021. Multilevel proteomics reveals host perturbations by SARS-CoV-2 and SARS-CoV. *Nature.* 594:246–252. https://doi.org/10.1038/s41586-021-03493-4

Surendran, H., S. Kumar, S. Narasimhaiah, A. Ananthamurthy, P.S. Varghese, G.A. D'Souza, G. Medigeshi, and R. Pal. 2022. SARS-CoV-2 infection of human-induced pluripotent stem cells-derived lung lineage cells evokes inflammatory and chemosensory responses by targeting mitochondrial

pathways. *J. Cell. Physiol.* 237:2913–2928. https://doi.org/10.1002/jcp.30755

Suzuki, H., M. Maeda, and K. Mihara. 2002. Characterization of rat TOM70 as a receptor of the preprotein translocase of the mitochondrial outer membrane. *J. Cell Sci.* 115:1895–1905. https://doi.org/10.1242/jcs.115.9.1895

Thorne, L.G., M. Bouhaddou, A.K. Reuschl, L. Zuliani-Alvarez, B. Polacco, A. Pelin, J. Batra, M.V.X. Whelan, M. Hosmillo, A. Fossati, et al. 2022. Evolution of enhanced innate immune evasion by SARS-CoV-2. *Nature.* 602:487–495. https://doi.org/10.1038/s41586-021-04352-y

Tyanova, S., T. Temu, and J. Cox. 2016. The MaxQuant computational platform for mass spectrometry-based shotgun proteomics. *Nat. Protoc.* 11: 2301–2319. https://doi.org/10.1038/nprot.2016.136

Weidberg, H., and A. Amon. 2018. MitoCPR-A surveillance pathway that protects mitochondria in response to protein import stress. *Science.* 360: eaan4146. https://doi.org/10.1126/science.aan4146

Wiertz, E.J., D. Tortorella, M. Bogyo, J. Yu, W. Mothes, T.R. Jones, T.A. Rapoport, and H.L. Ploegh. 1996. Sec61-mediated transfer of a membrane protein from the endoplasmic reticulum to the proteasome for destruction. *Nature.* 384:432–438. https://doi.org/10.1038/384432a0

Williamson, C.D., and A.M. Colberg-Poley. 2010. Intracellular sorting signals for sequential trafficking of human cytomegalovirus UL37 proteins to the endoplasmic reticulum and mitochondria. *J. Virol.* 84:6400–6409. https://doi.org/10.1128/JVI.00556-10

Wong, L.R., and S. Perlman. 2022. Immune dysregulation and immunopathology induced by SARS-CoV-2 and related coronaviruses—are we our own worst enemy? *Nat. Rev. Immunol.* 22:47–56. https://doi.org/10.1038/s41577-021-00656-2

Wu, Y., and B. Sha. 2006. Crystal structure of yeast mitochondrial outer membrane translocon member Tom70p. *Nat. Struct. Mol. Biol.* 13: 589–593. https://doi.org/10.1038/nsmb1106

Wu, J., Y. Shi, X. Pan, S. Wu, R. Hou, Y. Zhang, T. Zhong, H. Tang, W. Du, L. Wang, et al. 2021. SARS-CoV-2 ORF9b inhibits RIG-I-MAVS antiviral signaling by interrupting K63-linked ubiquitination of NEMO. *Cell Rep.* 34:108761. https://doi.org/10.1016/j.celrep.2021.108761

Yamamoto, H., K. Fukui, H. Takahashi, S. Kitamura, T. Shiota, K. Terao, M. Uchida, M. Esaki, S. Nishikawa, T. Yoshihisa, et al. 2009. Roles of Tom70 in import of presequence-containing mitochondrial proteins. *J. Biol. Chem.* 284:31635–31646. https://doi.org/10.1074/jbc.M109.041756

Young, J.C., N.J. Hoogenraad, and F.U. Hartl. 2003. Molecular chaperones Hsp90 and Hsp70 deliver preproteins to the mitochondrial import receptor Tom70. *Cell.* 112:41–50. https://doi.org/10.1016/S0092-8674(02)01250-3

Zanphorlin, L.M., T.B. Lima, M.J. Wong, T.S. Balbuena, C.A. Minetti, D.P. Remeta, J.C. Young, L.R.S. Barbosa, F.C. Gozzo, and C.H.I. Ramos. 2016. Heat shock protein 90 kDa (Hsp90) has a second functional interaction site with the mitochondrial import receptor Tom70. *J. Biol. Chem.* 291: 18620–18631. https://doi.org/10.1074/jbc.M115.710137

Supplemental material

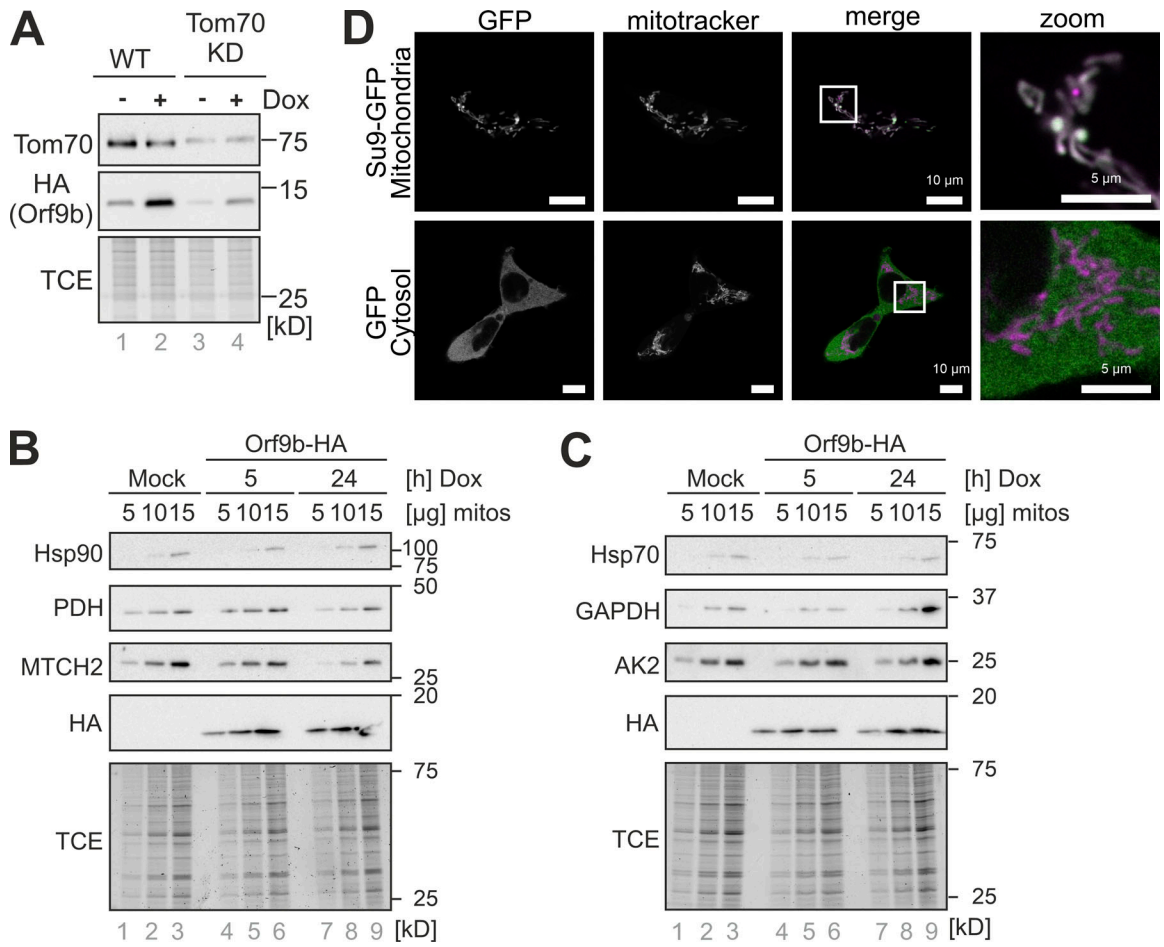

Figure S1. **Tom70 can be efficiently depleted in HEK293 cells. (A)** Tom70 was expressed in HEK293 cells. Orf9b expression was controlled by a doxycycline (Dox)-driven promoter. A total cell extract labeling with TCE is shown for control. Western blot signals of whole-cell extracts were analyzed with Tom70- and HA-specific antibodies. **(B and C)** Orf9b-HA expression was induced in galactose-grown HEK293 cells for 0, 5, and 24 h by addition of doxycycline (Dox). Mitochondria were isolated from these cells and analyzed by Western blotting using antibodies against the cytosolic chaperones Hsp70 and Hsp90, respectively, as well as antibodies against the mitochondrial proteins pyruvate dehydrogenase (PDH), MTCH2, adenylate kinase 2 (AK2) as well as the cytosolic enzyme GAPDH. **(D)** Mitochondria-targeted Su9-MTS-roGFP2 and cytosolic roGFP2-NES were expressed in HEK293 cells, fixated, and visualized by fluorescence microscopy. Signals were compared to those of MitoTracker. Scale bar = 10 µm. KD, knockdown. Source data are available for this figure: SourceData FS1.

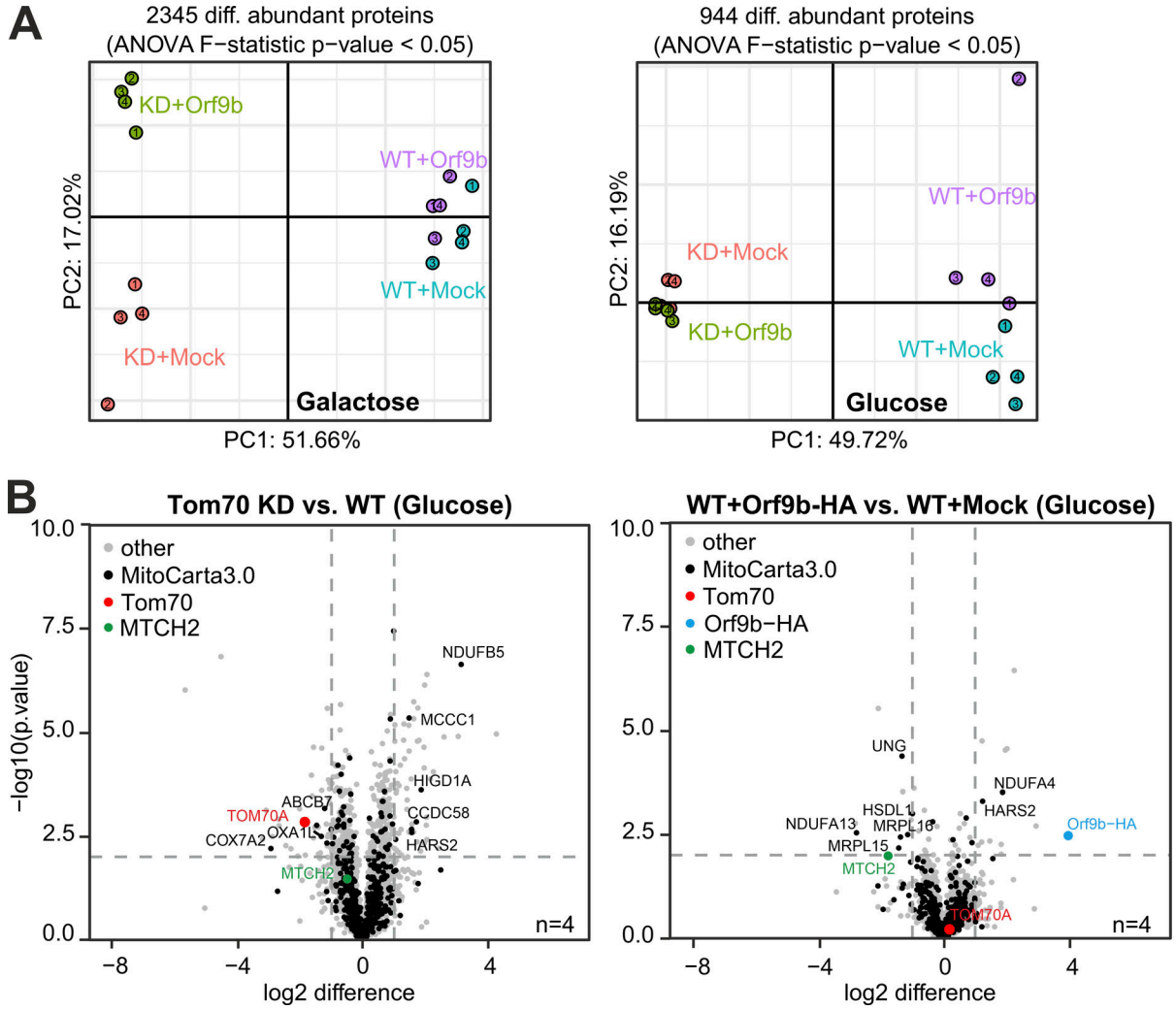

Figure S2. **The proteome of glucose-grown cells is only moderately affected by Tom70 depletion. (A)** Principal component (PC) analysis comparing the proteomes of the indicated cells. Principal component analysis was carried out for each data set on the relative abundance values of proteins with a discernable degree of variance between conditions as determined by an ANOVA F-statistic P value <0.05 between all four biological replicate groups. Samples located in proximity show similar protein abundance patterns regarding the first two principal components. Biological replicates therefore typically form clusters. The percentage of the overall variability in the data sets accounted for by the first and second principal components is indicated on the axis labels. **(B)** Volcano plots comparing the proteomes of glucose-grown cells. The $\log_2$ fold changes in protein abundances between the respective conditions are shown on the x axis, whereas the y axis reflects the significance of the changes as determined by Welch's *t* tests. Samples were analyzed as described in Fig. 2 A. KD, knockdown.

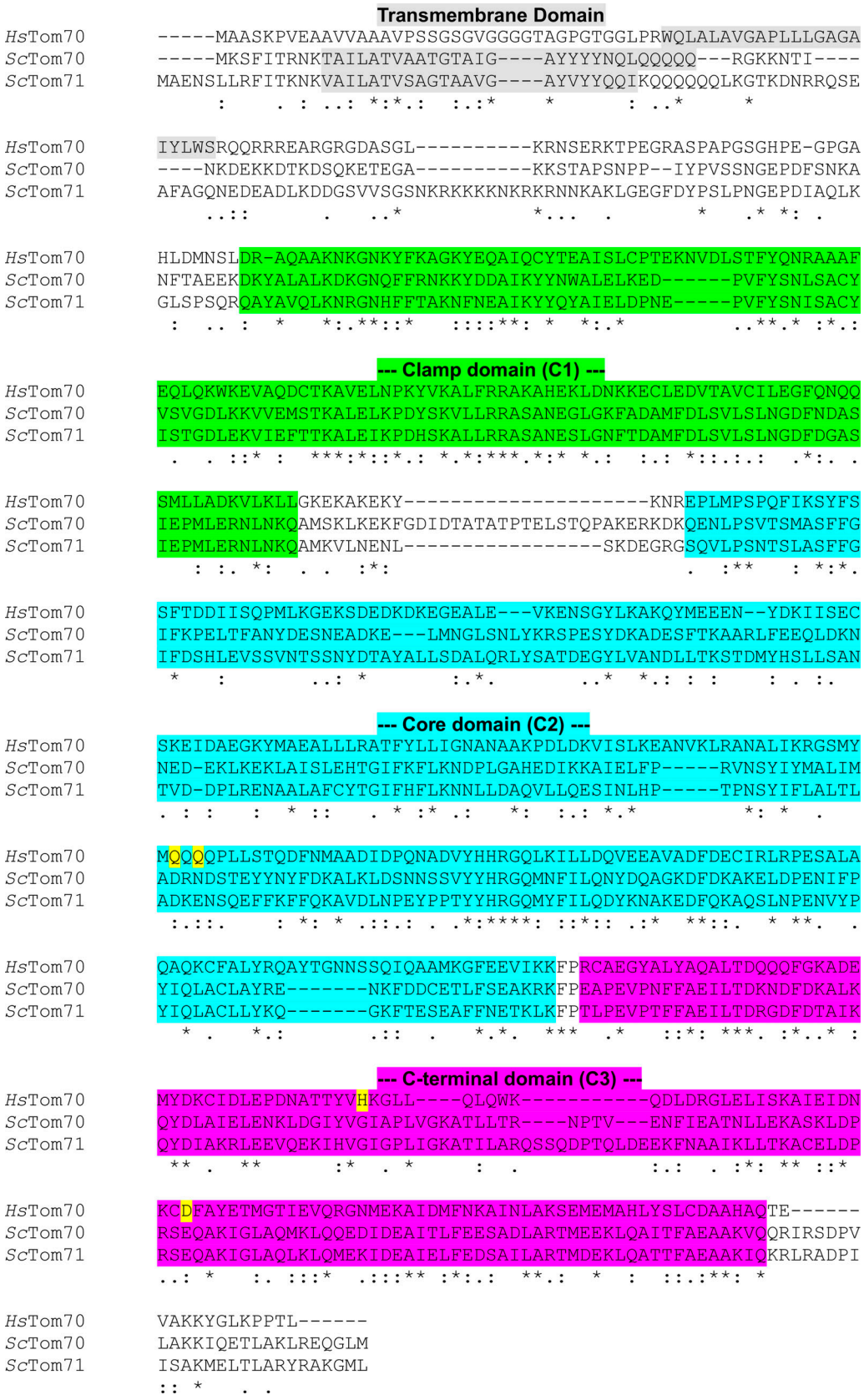

Figure S3. **Alignment of the sequences of Tom70 human and yeast homologs.** Shown are the sequences of *Hs*Tom70 (NP_055635.3), yeast Tom70 (*Sc*Tom70, NP_014278.3), and yeast Tom71 (*Sc*Tom71, AJU22976.1). The sequences were aligned using the Multiple Sequence Alignment tool Muscle using ClustalW as the output format and default settings (Edgar, 2004). The regions of the different Tom70 domains were indicated in consistence with previous studies (Young et al., 2003). The four residues in human Tom70 that mediate direct contact to bound Orf9b are highlighted in yellow (Gao et al., 2021).

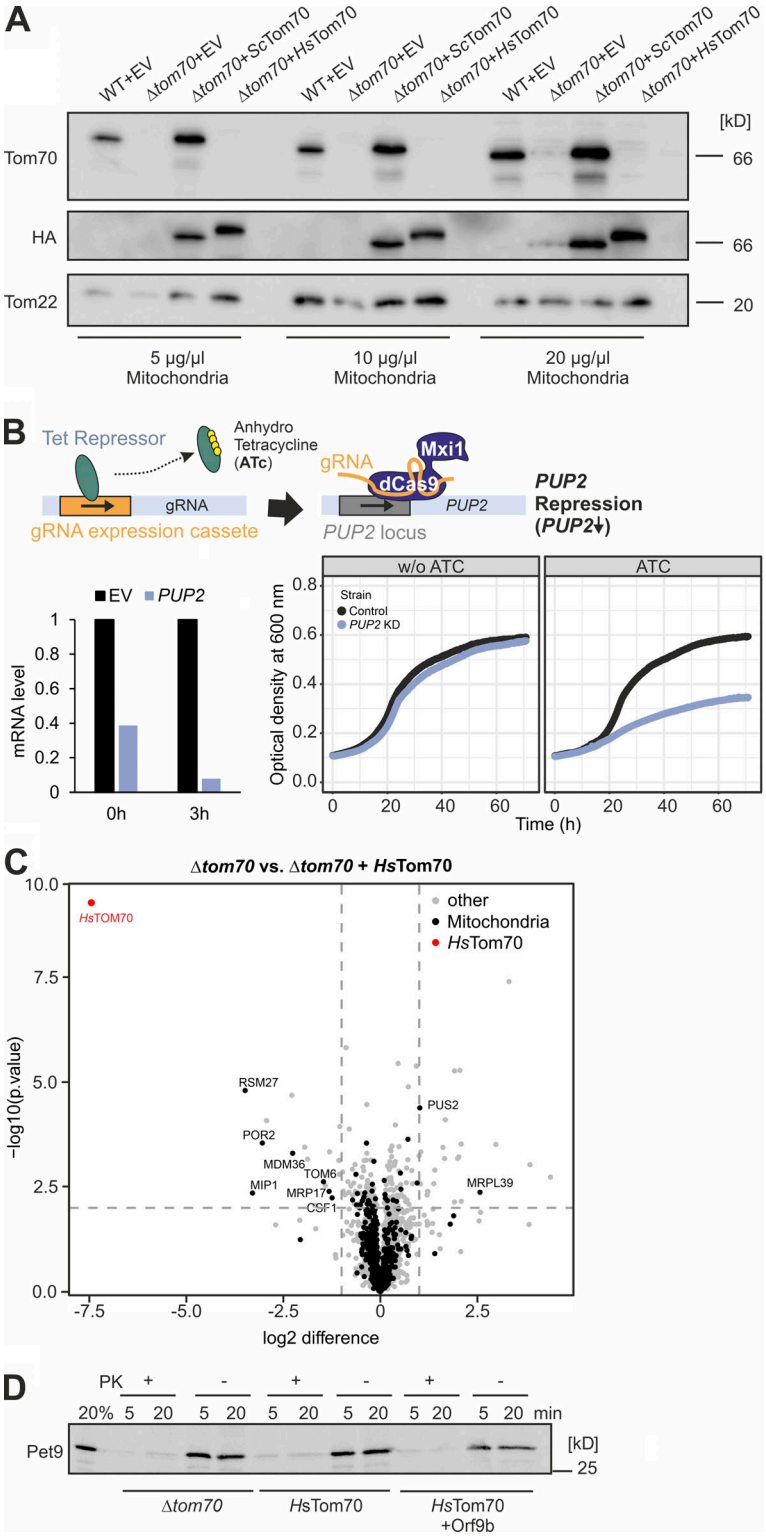

Figure S4. **The ATP/ADP carrier protein (Pet9) is not efficiently imported into mitochondria of semi-intact cells. (A)** Mitochondria were isolated from the WT and *Δtom70* cells containing an empty vector (EV) or plasmids for the expression of HA-tagged versions of the indicated Tom70 variants. The presence or absence of Tom70 was confirmed by Western blotting using antibodies against yeast Tom70, Tom22, and the HA epitope. **(B)** A schematic outline of the CRISPRi system for *PUP2* knockdown according to published procedures (Smith et al., 2016) is shown at the top. *PUP2* mRNA levels were measured by qPCR 3 h after addition of anhydrotetracycline (ATc) and are shown in comparison to an empty vector (EV) control. The growth of *PUP2* knock-down cells was compared with control cells after addition of 960 ng/µl ATc (bottom, right). **(C)** Same dataset as shown in Fig. 5 B. However, the scaling was adapted to show the position of *Hs*Tom70 in the graph. **(D)** Radiolabeled Pet9 was synthesized in reticulocyte lysate and incubated with semi-intact yeast cells of the strains indicated for 5 and 20 min. Non-imported protein was removed by treatment with PK. Note that basically all Pet9 proteins remained protease accessible. Source data are available for this figure: SourceData FS4.

Provided online are Table S1 and Table S2. Table S1 shows proteomic data from MS. Table S2 shows strains and plasmids.